

Topological susceptibility of $N_f = 2 + 1$ QCD from staggered fermions spectral projectors at high temperatures

Andreas Athenodorou,^{a,b} Claudio Bonanno,^{c,1} Claudio Bonati,^a Giuseppe Clemente,^d Francesco D'Angelo,^a Massimo D'Elia,^a Lorenzo Maio,^a Guido Martinelli,^e Francesco Sanfilippo^f and Antonino Todaro^{g,h,i}

^a *Università di Pisa and INFN Sezione di Pisa,
Largo B. Pontecorvo 3, I-56127 Pisa, Italy*

^b *Computation-based Science and Technology Research Center, The Cyprus Institute,
20 Kavafi Str., Nicosia 2121, Cyprus*

^c *INFN Sezione di Firenze,
Via G. Sansone 1, I-50019 Sesto Fiorentino, Firenze, Italy*

^d *Deutsches Elektronen-Synchrotron (DESY),
Platanenallee 6, 15738 Zeuthen, Germany*

^e *Dipartimento di Fisica and INFN Sezione di Roma “La Sapienza”,
Piazzale Aldo Moro 5, I-00185 Rome, Italy*

^f *INFN Sezione di Roma Tre,
Via della Vasca Navale 84, I-00146 Rome, Italy*

^g *Department of Physics, University of Cyprus,
P.O. Box 20537, 1678 Nicosia, Cyprus*

^h *Faculty of Mathematics and Natural Sciences, University of Wuppertal,
Wuppertal-42119, Germany*

ⁱ *Dipartimento di Fisica, Università di Roma “Tor Vergata”,
Via della Ricerca Scientifica 1, I-00133 Rome, Italy*

E-mail: a.athenodorou@cyi.ac.cy, claudio.bonanno@fi.infn.it,
claudio.bonati@unipi.it, giuseppe.clemente@desy.de,
francesco.dangelo@phd.unipi.it, massimo.delia@unipi.it,
lorenzo.maio@phd.unipi.it, guido.martinelli@roma1.infn.it,
francesco.sanfilippo@infn.it, atodar01@ucy.ac.cy

ABSTRACT: We compute the topological susceptibility of $N_f = 2 + 1$ QCD with physical quark masses in the high-temperature phase, using numerical simulations of the theory discretized on a space-time lattice. More precisely we estimate the topological susceptibility

¹Corresponding author.

for five temperatures in the range from ~ 200 MeV up to ~ 600 MeV, adopting the spectral projectors definition of the topological charge based on the staggered Dirac operator. This strategy turns out to be effective in reducing the large lattice artifacts which affect the standard gluonic definition, making it possible to perform a reliable continuum extrapolation. Our results for the susceptibility in the explored temperature range are found to be partially in tension with previous determinations in the literature.

KEYWORDS: Lattice QCD, Vacuum Structure and Confinement, Axions and ALPs, CP Violation

ARXIV EPRINT: [2208.08921](https://arxiv.org/abs/2208.08921)

Contents

1	Introduction	1
2	Numerical setup	4
2.1	Lattice action	4
2.2	Topological charge discretizations	5
2.3	Multicanonical algorithm	8
3	Results	9
3.1	Topological susceptibility at zero temperature	9
3.2	Topological susceptibility at finite temperature	13
3.3	$\chi(T)$ from spectral projectors and comparison with the DIGA	18
4	Conclusions	21
A	Summary of finite temperature results for χ	23
A.1	$T = 230$ MeV	24
A.2	$T = 300$ MeV	25
A.3	$T = 365$ MeV	26
A.4	$T = 570$ MeV	27

1 Introduction

The study of the topological properties of QCD at high temperatures is of utmost importance not only to provide better insight into the non-perturbative regime of this theory, but also because of its phenomenological implications for axion physics and cosmology. This justifies the interest in this topic, which has been the subject of several recent Lattice QCD investigations [1–6].

The axion is an hypothetical particle whose existence is predicted by the Peccei-Quinn solution of the strong CP-problem [7–10], that was also early recognized as a possible Dark Matter candidate. Since the axion is directly coupled to the topological charge Q defined by ($F^{\mu\nu}$ is the QCD field strength)

$$Q = \frac{1}{32\pi^2} \varepsilon_{\mu\nu\rho\sigma} \int \text{Tr} \{F^{\mu\nu}(x)F^{\rho\sigma}(x)\} d^4x, \tag{1.1}$$

the axion square mass is proportional to the topological susceptibility $\chi = \langle Q^2 \rangle / V$ (V is the four-dimensional space-time volume). More precisely $m_a^2 = \chi / f_a^2$, where f_a is the *a priori* unknown axion coupling scale. An important peculiarity of axion physics is that it is possible, modulo some general cosmological assumptions, to put an *upper* bound on the energy scale f_a [11–13]. The specific value of this upper bound is fixed by the present time Dark Matter abundance and by the temperature dependence of the axion effective potential,

i.e., mainly by the temperature dependence of the QCD topological susceptibility χ . Since an upper bound on f_a provides a lower bound for the axion mass, the study of the QCD topological observables at finite temperature provides an essential input for current and future experimental axion searches (see [14] for a recent review of the experimental bounds).

When the temperature is asymptotically high, one can compute $\chi(T)$ by combining semiclassical methods and perturbation theory. Assuming instantons to be well separated and thus approximately not interacting with each other (Dilute Instanton Gas Approximation, DIGA for short), and performing a one loop computation in an instanton background, it is possible to obtain the result [15, 16]:

$$\chi(T) \propto T^{-c}, \quad c = \frac{11}{3}N_c + \frac{1}{3}N_f - 4, \quad (1.2)$$

where a logarithmic dependence of χ on the temperature has been implied and N_c, N_f are the number of colors and light flavors respectively. Being based on a combination of semiclassical and perturbative approximations, this result is expected to be trustworthy only for $T \gg \Lambda_{\text{QCD}} \approx T_c$. Nevertheless, due to the absence of more reliable computations, this result has been routinely used to estimate the cosmological axion relic density needed to constrain the axion coupling f_a . In performing this computation the expression of $\chi(T)$ has however to be used starting from $T \gg T_c$ but reaching temperatures of the order of $1 \div 10$ GeV (see, e.g., ref. [17]), where non-perturbative deviations from the asymptotic high- T regime could be relevant. To avoid introducing systematic errors in the computation of the axion coupling bound, it was thus suggested to use first principles Lattice QCD results for $\chi(T)$ instead of the corresponding DIGA expression [18].

When exploring the high temperature regime of QCD with lattice simulations, there are however several nontrivial numerical problems that have to be faced. Among them the most notable are:

(i) *Rare $|Q| > 0$ events*

The topological susceptibility drops very rapidly with the temperature (DIGA predicts $c \approx 8$ for 3 light flavors, cf. eq. (1.2)), thus the probability of visiting configurations with $Q \neq 0$ is rapidly suppressed as the temperature is increased. This sampling problem has a physical origin and can be understood in terms of the vanishing of the variance of the topological charge probability distribution $P(Q)$: since $\langle Q^2 \rangle = \chi V \ll 1$ on affordable volumes, we have $P(Q = 0) \gg P(|Q| > 0)$. From the numerical point of view, this implies the necessity of collecting very large statistics in order to observe a sufficient number of fluctuations above zero to reliably compute χ .

(ii) *Explicit breaking of chiral symmetry and large lattice artifacts*

According to the *index theorem*, the appearance of zero-modes in the spectrum of the continuum massless Dirac operator \not{D} is related to the topological charge Q of the background gauge field:

$$Q = n_+ - n_-, \quad (1.3)$$

where n_+ (n_-) is the number of zero modes with positive (negative) chirality. For this reason, a finite volume configuration with non-zero topological charge enters the

continuum path integral with a weight that is suppressed in the chiral limit as a power of the light quark mass. On the lattice, however, if the sea quark discretization explicitly breaks the chiral symmetry, no zero mode is present and no mode is chiral, being the smallest eigenvalues shifted by cut-off effects. Such Would-Be Zero Modes (WBZMs) make the suppression of $Q \neq 0$ configurations less efficient compared to the continuum. As a consequence the numerical determination of χ is affected by large lattice artifacts, and its continuum extrapolation requires particular care in the analysis of systematic uncertainties. In principle this issue could be solved by simulating extremely fine lattice spacings, which is in practice prevented by the *topological critical slowing down* problem.

(iii) *Topological critical slowing down*

Local updating algorithms, such as the Rational Hybrid Monte Carlo (RHMC) [19, 20], become less and less effective in changing the topological charge of the configurations as the lattice spacing is decreased. While the critical slowing down generically affects all observables, it is particularly severe for the topological observables, for which the increase of the autocorrelation time is consistent with an exponential in the inverse lattice spacing [21–26]. In practice, if the lattice spacing is small enough ergodicity is lost and the whole Monte Carlo simulation remains trapped in the same topological sector; as a matter of fact, this problem is also referred to as the “freezing problem”. This makes extremely difficult to reach, for the temperatures studied in this work, lattice spacings of the order or smaller than 0.01 fm.

Overcoming these issues is mandatory to provide reliable lattice computations of $\chi(T)$ at high temperatures, and several different strategies have been proposed in literature to this end. For instance, in ref. [3] (see also [2]), the authors compute $\chi(T)$ bypassing issues (i) and (iii) simultaneously by restricting only to $Q = 0$ and $|Q| = 1$, where neglecting contributions from higher-charge sectors is justified on the basis of the DIGA itself. The computational problem (ii), related to the adoption of staggered fermions in the lattice action, was instead addressed in ref. [3] by reweighting configurations according to their expected continuum lowest eigenvalues of \not{D} , thus trying to correct *a posteriori* for the inaccurate sampling of chiral modes. A crucial point to perform such a reweighting is the determination of WBZMs, that are not so easily distinguishable from non-chiral modes without some extra assumptions due to the explicit breaking of chiral symmetry on the lattice.

The main goal of this work is to make progress towards an independent determination of $\chi(T)$ in full QCD from the lattice without any extra *ad hoc* hypothesis. In particular, we will compute this quantity in $N_f = 2 + 1$ QCD at the physical point combining the two following strategies:

(a) *Topological susceptibility from staggered fermions spectral projectors*

In order to reduce the magnitude of lattice artifacts, we adopt a definition of the topological susceptibility based on the Spectral Projectors (SP) method [27–31], introduced for staggered fermions in ref. [32]. This discretization, based on a lattice

version of the index theorem, consists of defining Q as the sum of the chiralities of all the modes lying below a certain threshold M . The SP topological susceptibility is a theoretically well-defined quantity, as it can be shown to converge to the correct continuum limit, and the choice of M can be used to reduce the lattice artefacts with respect to the standard gluonic definition of the topological charge. Our approach will allow us to have a better control on the systematic uncertainties related to the continuum extrapolation of χ already in the lattice spacing range employed in typical simulations, thus alleviating the necessity for extremely fine lattice spacings to reduce lattice artifacts, whose use would require a specific strategy to deal with the issue (iii).

(b) *Multicanonical algorithm*

The multicanonical algorithm [33] was introduced to study strong first order phase transitions, and was adapted in [5, 25, 34, 35] to deal with the problem of the dominance of the $Q = 0$ sector at high temperatures (issue (i) above). The idea is to add to the lattice action a fixed (as opposed to the case of metadynamics [36]) bias topological potential in order to enhance the probability of visiting suppressed topological sectors, thus effectively enhancing the fluctuations of Q during the Monte Carlo evolution. Expectation values with respect to the original path-integral distribution are then exactly reproduced by using standard reweighting. With respect to the standard approach, in this way a much better statistical accuracy is achieved in the determination of the relative weights of the topological sectors.

We here anticipate that our results for $\chi(T)$ obtained from spectral projectors show some difference with respect to those reported in ref. [3], as we observe a $\sim 2 - 3$ standard deviation tension in a temperature range between 300 and 400 MeV. We also observe, in the same temperature range, a milder $\sim 2 - 2.5$ standard deviation tension with respect to the determinations of ref. [4], which however had to be mass-extrapolated to be compared with our results, as will be discussed in the following.

This paper is organized as follows: in section 2 we present our numerical setup, discussing in particular the spectral discretization of the topological susceptibility (a) and our implementation of the multicanonical algorithm (b). In section 3 we present continuum-extrapolated results for the topological susceptibility in $N_f = 2 + 1$ QCD at the physical point. First, we apply the SP approach to the $T = 0$ case, which is used as a test-bed to compare this method with the standard gluonic approach. Then, we adopt the same SP method in combination with the multicanonical approach to compute the topological susceptibility as a function of the temperature in the range $200 \text{ MeV} \lesssim T \lesssim 600 \text{ MeV}$. Our results are then compared with other determinations in the literature and with DIGA predictions. Finally, in section 4 we draw our conclusions and discuss future outlooks of this work.

2 Numerical setup

2.1 Lattice action

We discretize $N_f = 2 + 1$ QCD on a $N_s^3 \times N_t$ lattice adopting rooted stouted staggered fermions for the quark sector and the tree-level Symanzik improved gauge action for the

gluon sector. The partition function Z_{LQCD} is thus given by

$$Z_{\text{LQCD}} = \int [dU] e^{-S_{\text{YM}}^{(L)}[U]} \det \left\{ \mathcal{M}_l^{(\text{stag})}[U] \right\}^{\frac{1}{2}} \det \left\{ \mathcal{M}_s^{(\text{stag})}[U] \right\}^{\frac{1}{4}}, \quad (2.1)$$

where $u = d \equiv l$ and s denote the two mass-degenerate light quarks and the strange quark respectively. The staggered Dirac operator D_{stag} is defined by using the gauge links $U_\mu^{(2)}$, obtained by applying to the gauge configuration $n_{\text{stout}} = 2$ levels of isotropic stout smearing [37] with $\rho_{\text{stout}} = 0.15$, thus:

$$\begin{aligned} \mathcal{M}_f^{(\text{stag})}[U] &\equiv D_{\text{stag}}[U^{(2)}] + \hat{m}_f, & \hat{m}_f &\equiv am_f, \\ D_{\text{stag}}[U^{(2)}] &= \sum_{\mu=1}^4 \eta_\mu(x) \left(U_\mu^{(2)}(x) \delta_{x,y-\hat{\mu}} - U_\mu^{(2)\dagger}(x-\hat{\mu}) \delta_{x,y+\hat{\mu}} \right), \\ \eta_\mu(x) &= (-1)^{x_1+\dots+x_{\mu-1}}. \end{aligned} \quad (2.2)$$

The tree-level Symanzik-improved Wilson action is instead expressed in terms of the non-stouted gauge links:

$$S_{\text{YM}}^{(L)}[U] = -\frac{\beta}{3} \sum_{x,\mu \neq \nu} \left\{ \frac{5}{6} \Re \text{Tr} \left[\Pi_{\mu\nu}^{(1 \times 1)}(x) \right] - \frac{1}{12} \Re \text{Tr} \left[\Pi_{\mu\nu}^{(1 \times 2)}(x) \right] \right\}, \quad (2.3)$$

where $\Pi_{\mu\nu}^{(n \times m)}(x)$ is the $n \times m$ Wilson loop.

The bare parameters β , \hat{m}_s and $\hat{m}_u = \hat{m}_d \equiv \hat{m}_l$ are tuned in order to move on a Line of Constant Physics (LCP) corresponding to the physical values of the pion mass $m_\pi \simeq 135$ MeV and of the ratio $\hat{m}_s/\hat{m}_l = m_s/m_l \simeq 28.15$ [38–40].

2.2 Topological charge discretizations

Topological charge definitions can be divided into two broad groups: gluonic and fermionic ones. The simplest gluonic definition is the clover one, which is a straightforward discretization of eq. (1.1) with definite parity [41, 42]:

$$Q_{\text{clov}} = \frac{-1}{2^9 \pi^2} \sum_x \sum_{\mu\nu\rho\sigma=\pm 1}^{\pm 4} \varepsilon_{\mu\nu\rho\sigma} \text{Tr} \left\{ \Pi_{\mu\nu}^{(1 \times 1)}(x) \Pi_{\rho\sigma}^{(1 \times 1)}(x) \right\}, \quad (2.4)$$

where $\Pi_{\mu\nu}^{(1 \times 1)}(x)$ is the plaquette and the Levi-Civita symbol with negative entries is defined by $\varepsilon_{\mu\nu\rho\sigma} = -\varepsilon_{(-\mu)\nu\rho\sigma}$ and complete antisymmetry. When computing the susceptibility $\chi = \langle Q^2 \rangle / V$ using Q_{clov} , both multiplicative [43] and additive renormalizations appear:¹

$$\chi_{\text{gluo}} = Z_Q^2 \frac{\langle Q_{\text{clov}}^2 \rangle}{V} + M_{\text{add}}. \quad (2.5)$$

Such renormalizations are due to ultraviolet (UV) fluctuations at the scale of the lattice spacing and must be properly subtracted in order to recover the proper continuum scaling of χ_{gluo} . To avoid dealing with these renormalization constants, smoothing algorithms are

¹The same is true for all the “non geometric” gluonic definitions of the topological charge [44].

commonly employed to dampen UV fluctuations while leaving the topological content of the gauge fields unchanged. Several methods have been proposed, such as cooling [45–51], smearing [37, 52] and gradient flow [53, 54], all giving consistent results when properly matched [51, 55, 56].

To compute the gluonic susceptibility, in this work we adopt the cooling method, which is numerically very convenient. Since even after cooling the topological charge is non-integer (although its typical values get closer and closer to integers as the lattice spacing is reduced) we adopt the following prescription to assign an integer topological charge to configurations [57, 58]:

$$Q_{\text{gluo}} = \text{round} \left\{ \alpha Q_{\text{clov}}^{(\text{cool})} \right\}, \quad (2.6)$$

where “round” means that the quantity $\alpha Q_{\text{clov}}^{(\text{cool})}$ is rounded to the closest integer and where the parameter α is defined by

$$\alpha = \min_{x \geq 1} \left\langle \left[x Q_{\text{clov}}^{(\text{cool})} - \text{round} \left\{ x Q_{\text{clov}}^{(\text{cool})} \right\} \right]^2 \right\rangle. \quad (2.7)$$

The parameter α is thus chosen in order to center the peaks of the distribution of $\alpha Q_{\text{clov}}^{(\text{cool})}$ at integer values, and the constraint $x \geq 1$ is required to exclude the trivial minimum $x = 0$. In the end, our gluonic susceptibility is:

$$\chi_{\text{gluo}} = \frac{\langle Q_{\text{gluo}}^2 \rangle}{V}, \quad V = a^4 N_t N_s^3. \quad (2.8)$$

In our simulations we observe that after $n_{\text{cool}} \sim 100$ cooling steps χ_{gluo} has reached a plateau for all explored lattice spacings. For this reason, we compute the gluonic susceptibility for that number of cooling steps in all cases. Slightly changing the value of n_{cool} resulted in no change in the obtained results for χ_{gluo} for each lattice spacing.

It is also possible to adopt fermionic definitions of the topological charge, based on the properties of the spectrum of the lattice Dirac operator. In the continuum limit, according to the index theorem, it would be sufficient to compute the sum of the chiralities of the zero-modes u_0 , as

$$Q = \text{Tr} \{ \gamma_5 \} = \sum_{\text{zero modes}} u_0^\dagger \gamma_5 u_0 = n_+ - n_-. \quad (2.9)$$

On the lattice, since no exact zero-mode exists when using a non-chiral fermion discretization, every mode contributes and the trace becomes a sum over all modes. To properly define the topological charge, we introduce the projector on the eigenspace spanned by the eigenstates of $iD_{\text{stag}}[U^{(2)}]$ (i.e., the same operator we have included in our lattice action) with eigenvalues $|\lambda| \leq M$:

$$\mathbb{P}_M \equiv \sum_{|\lambda| \leq M} u_\lambda u_\lambda^\dagger, \quad iD_{\text{stag}}[U^{(2)}] u_\lambda = \lambda u_\lambda, \quad \lambda \in \mathbb{R}. \quad (2.10)$$

Our SP definition of the bare topological charge is:

$$Q_{\text{SP,bare}}^{(\text{stag})} = \frac{1}{n_t} \text{Tr} \{ \Gamma_5 \mathbb{P}_M \} = \frac{1}{n_t} \sum_{|\lambda| \leq M} u_\lambda^\dagger \Gamma_5 u_\lambda, \quad \Gamma_5 = \gamma_5^{(\text{stag})}, \quad (2.11)$$

where the factor $n_t = 2^{d/2} = 2^2$ takes into account the taste degeneration of the staggered spectrum.

As discussed in ref. [32], this definition is affected only by a multiplicative renormalization, since the fast decay of the spectral projector at infinity eliminates any additive renormalization. This multiplicative constant can be expressed in terms of traces of Γ_5 and of the spectral projector \mathbb{P}_M , thus, we are able to obtain a fully-spectral renormalized definition of the topological charge [32]:

$$Q_{\text{SP}}^{(\text{stag})} = Z_{\text{SP}}^{(\text{stag})} Q_{\text{SP,bare}}^{(\text{stag})}, \quad (2.12)$$

$$Z_{\text{SP}}^{(\text{stag})} = \sqrt{\frac{\langle \text{Tr} \{ \mathbb{P}_M \} \rangle}{\langle \text{Tr} \{ \Gamma_5 \mathbb{P}_M \Gamma_5 \mathbb{P}_M \} \rangle}}. \quad (2.13)$$

The SP expression of the topological susceptibility can then be written as

$$\chi_{\text{SP}}^{(\text{stag})} = Z_{\text{SP}}^{(\text{stag})2} \frac{\langle Q_{\text{SP,bare}}^{(\text{stag})2} \rangle}{V} = \frac{1}{n_t^2} \frac{\langle \text{Tr} \{ \mathbb{P}_M \} \rangle}{\langle \text{Tr} \{ \Gamma_5 \mathbb{P}_M \Gamma_5 \mathbb{P}_M \} \rangle} \frac{\langle \text{Tr} \{ \Gamma_5 \mathbb{P}_M \}^2 \rangle}{V}. \quad (2.14)$$

Spectral traces can be computed by several means. For example, in refs. [28, 29] noisy estimators are used to this end. In this work we follow the same strategy of ref. [32] and we compute the first 200 smallest eigenvalues and eigenvectors of $iD_{\text{stag}}[U^{(2)}]$ using the PARPACK package [59], so that \mathbb{P}_M is obtained directly from eq. (2.10). On our larger lattices, the computational cost to obtain the 200 lowest-lying eigenvalues of $iD_{\text{stag}}[U^{(2)}]$ turned out to be about a factor of ~ 20 larger than the computational cost needed to perform a single RHMC step for the same lattice.

Once the eigenvalues and the eigenvectors of $iD_{\text{stag}}[U^{(2)}]$ are obtained, spectral traces are then practically computed as follows:

$$\begin{aligned} \text{Tr} \{ \mathbb{P}_M \} &= \sum_{|\lambda| \leq M} 1 = \nu(M), \\ \text{Tr} \{ \Gamma_5 \mathbb{P}_M \} &= \sum_{|\lambda| \leq M} u_\lambda^\dagger \Gamma_5 u_\lambda, \\ \text{Tr} \{ \Gamma_5 \mathbb{P}_M \Gamma_5 \mathbb{P}_M \} &= \sum_{|\lambda| \leq M} \sum_{|\lambda'| \leq M} |u_\lambda^\dagger \Gamma_5 u_{\lambda'}|^2, \end{aligned} \quad (2.15)$$

where $\nu(M)$ is the total number of eigenmodes whose eigenvalues lie below M .

The cut-off mass M is a free parameter, and from the index theorem we know that its specific value is irrelevant in the continuum limit. However, M should be kept constant in physical units as the continuum limit is approached in order to observe the usual continuum scaling of the susceptibility (i.e., $O(a^2)$ corrections in the staggered case), as discussed in ref. [28]. The cut-off mass renormalizes as a quark mass [32], i.e., $M_R = Z_S^{-1} M$, where Z_S is the renormalization constant of the staggered flavor-singlet scalar fermionic density. For this reason, the ratio between M and any of the quark masses is a renormalization-group invariant quantity: $M/m_f = M_R/m_f^{(R)}$. To keep M_R constant in physical units, it is thus sufficient to keep $\hat{M}/\hat{m}_f = M/m_f$ constant as we move \hat{m}_f along the LCP (where $\hat{M} \equiv aM$). This strategy allows to completely avoid the computation of Z_S and will be

the one adopted in this work. When the continuum limit is taken at fixed M/m_f , we thus expect the usual scaling:

$$\chi_{\text{SP}}^{(\text{stag})}(a, M/m_f) = \chi_{\text{SP}} + c_{\text{SP}}(M/m_f) a^2 + o(a^2). \quad (2.16)$$

Previous studies of QCD at zero temperature, performed with twisted mass Wilson fermions and using twisted mass Wilson SP, have shown that the SP determination of the topological susceptibility displays much smaller lattice artifacts than the gluonic one [31]. Although we still do not have a complete quantitative understanding of this fact, an intriguing possible interpretation exists (see also the discussion at the end of ref. [32]). When using a non-chiral fermion discretization we are sampling a lattice distribution that, for what concerns the low-lying modes relevant for topology, can have quite large lattice artifacts due to the explicit chiral symmetry breaking. If we use a gluonic definition of the topological charge, we have lost any direct connection with lattice chirality and the error introduced in the sampling propagates to the measures. If instead we use the SP definition built from the same Dirac operator used to weight the configurations, there is the possibility that the measure partially corrects the error in the sampling. Of course there is *a priori* no solid reason to exclude the possibility that the two different errors sum up instead of canceling each other, so this argument can not be considered in the present form conclusive. To understand to what extent such a cancellation exists, it would be very interesting to perform a study using different fermion discretizations in the generation of the configuration and in the construction of the SP used to estimate the topological charge.

As a final remark we recall that, as already discussed in ref. [32], at finite temperature a possible ambiguity about the computation of the renormalization constant in eq. (2.13) could arise. In particular, one could wonder if $Z_{\text{SP}}^{(\text{stag})}$ should be computed at finite T or at zero T . In principle, such quantity should be computed in the latter case, which would require to perform, along each finite temperature simulation, a twin run with the same parameters but at zero temperature to compute $Z_{\text{SP}}^{(\text{stag})}$. However, as already discussed in ref. [32] in the quenched theory and as we will verify also in the following in the presence of dynamical fermions, the computation of $\chi_{\text{SP}}^{(\text{stag})}$ at finite temperature gives fully consistent results both when $Z_{\text{SP}}^{(\text{stag})}$ is obtained from the same finite- T ensemble employed for the computation of $Q_{\text{SP}}^{(\text{stag})}$ or from a corresponding ensemble at zero temperature, as long as the spectral traces appearing in eq. (2.13) are computed from the staggered spectrum obtained imposing periodic boundaries along the temporal direction for D_{stag} .² Thus, in our finite temperature simulations, we will compute the spectrum of the Dirac operator both for periodic and anti-periodic boundary conditions along the temporal direction, and in eq. (2.14) we will adopt the former to compute $Z_{\text{SP}}^{(\text{stag})}$ and the latter to compute $Q_{\text{SP,bare}}^{(\text{stag})}$.

2.3 Multicanonical algorithm

The multicanonical approach consists in adding a topological bias potential $V_{\text{topo}}(Q_{\text{mc}})$ to the action in order to enhance the probability of visiting those topological sectors that

²On the other hand, at zero temperature the choice of boundary conditions for the lattice Dirac operator along the temporal direction is expected to be irrelevant.

would be otherwise strongly suppressed:

$$S_{\text{YM}}^{(L)} \rightarrow S_{\text{YM}}^{(L)} + V_{\text{topo}}(Q_{\text{mc}}). \quad (2.17)$$

The quantity Q_{mc} is a suitable discretization of the topological charge, which in general differs from the one adopted for the measurements Q_{gluo} . While the multicanonical algorithm is stochastically exact for any choice of Q_{mc} , to make it more efficient than the case $V_{\text{topo}} = 0$ the discretization Q_{mc} has to satisfy a couple of requirements. First, Q_{mc} must have a reasonable overlap with the charge used in the measures, otherwise $V_{\text{topo}}(Q_{\text{mc}})$ would not work as a bias but just as noise. Second, it is also important that Q_{mc} is not “too peaked” at integer values, to avoid the need for very small integration steps in the Hybrid Monte Carlo.

The partition function in the presence of the topological potential $Z_{\text{LQCD}}^{(\text{mc})}$ is the following:

$$Z_{\text{LQCD}}^{(\text{mc})} = \int [dU] e^{-\left(S_{\text{YM}}^{(L)}[U] + V_{\text{topo}}(Q_{\text{mc}})\right)} \det \left\{ \mathcal{M}_l^{(\text{stag})}[U] \right\}^{\frac{1}{2}} \det \left\{ \mathcal{M}_s^{(\text{stag})}[U] \right\}^{\frac{1}{4}}. \quad (2.18)$$

For a generic observable \mathcal{O} , expectation values with respect to the original path-integral distribution $\langle \mathcal{O} \rangle$ can thus be exactly recovered through a simple reweighting procedure:

$$\langle \mathcal{O} \rangle = \frac{\langle \mathcal{O} e^{V_{\text{topo}}(Q_{\text{mc}})} \rangle_{\text{mc}}}{\langle e^{V_{\text{topo}}(Q_{\text{mc}})} \rangle_{\text{mc}}}, \quad (2.19)$$

where $\langle \cdot \rangle_{\text{mc}}$ refers to expectation values computed in the presence of the topological bias.

3 Results

3.1 Topological susceptibility at zero temperature

At zero temperature, the value of the topological susceptibility in QCD can be reliably computed using Chiral Perturbation Theory (ChPT) [60–65], and the value obtained in this way constitutes a useful benchmark for lattice determinations. Using the Next-to-Leading Order (NLO) expression of ref. [64] one gets for the case $m_u = m_d$ at the physical point the estimate [1]:

$$\chi_{\text{ChPT}}^{1/4} = 77.8(4) \text{ MeV}, \quad (m_u/m_d = 1). \quad (3.1)$$

Moreover, several gluonic determinations from the lattice have been reported in the literature, see, e.g., refs. [1, 3]. We will use the computation of the zero temperature topological susceptibility as a test to validate our implementation, and to verify that the spectral projector approach has significantly smaller lattice artifacts than the standard gluonic one.

Our zero-temperature simulations have been performed on hypercubic N_s^4 lattices and the simulation parameters adopted are reported in table 1. The lattice size was chosen so that $L_s \equiv aN_s \sim 2.6\text{--}3.2 \text{ fm}$, which is sufficient to keep finite-size effects within our typical statistical errors [1]. At zero temperature, there is no need to introduce a bias potential in the action, since several topological sectors are naturally explored during the Monte Carlo evolution. As an example, we show the history of the topological charge Q_{gluo} for our finest lattice spacing in figure 1.

β	a [fm]	$\hat{m}_s \cdot 10^2$	N_s
3.750	0.1249	5.03	24
3.850	0.0989	3.94	32
3.938	0.0824	3.30	32
4.020	0.0707	2.81	40
4.140	0.0572	2.24	48

Table 1. Summary of simulation parameters for the $T \simeq 0$ runs, performed on hypercubic N_s^4 lattices. The bare parameters β and \hat{m}_s and the lattice spacings have been fixed according to the LCP determined in refs. [38–40], and \hat{m}_l is fixed through $\hat{m}_s/\hat{m}_l = m_s/m_l = 28.15$.

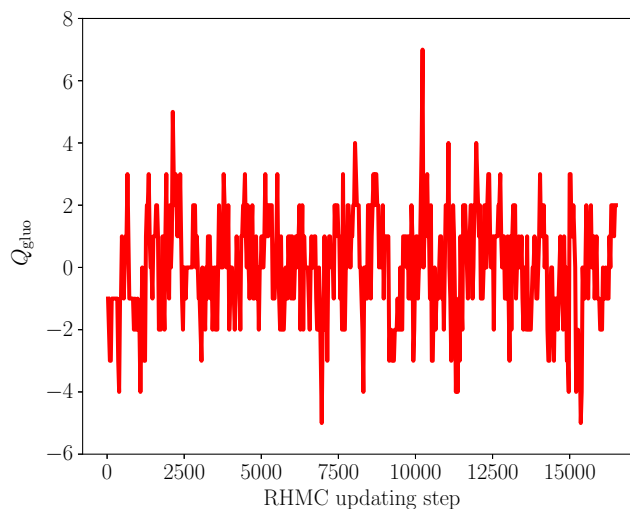


Figure 1. Monte Carlo history of Q_{gluo} , defined in eq. (2.6), for our run with $\beta = 4.140$ at $T \simeq 0$, corresponding to the finest lattice spacing explored at this temperature.

To compute χ using spectral projectors we have to choose the cut-off mass M , which in the following computations will be normalized to the strange quark mass m_s . Since we know that in the continuum limit only zero modes provide a non-vanishing contribution to the topological charge, *a priori* the optimal possibility would be to fix a value of M/m_s large enough to include in the spectral sums in eqs. (2.15) all the Would-Be Zero Modes (WBZMs) of all the configurations, but small enough to leave out all the other modes that become irrelevant in the continuum. In general, whether this “golden choice” of M/m_s exists or not depends on the amount of explicit chiral symmetry breaking of the fermion discretization. However, in the $T = 0$ case we can already guess that such a sharp separation can not be present in the spectrum. Indeed, due to the Banks-Casher relation, the spontaneous breaking of chiral symmetry is associated to a proliferation of near-zero modes.

Using for the eigenmodes and the eigenvalues of $iD_{\text{stag}}[U^{(2)}]$ the notation u_λ and λ respectively (cf. eq. (2.10)), we can associate to each mode its (absolute) chirality $r_\lambda \equiv |u_\lambda^\dagger \Gamma_5 u_\lambda|$. In the continuum $r_\lambda = 1$ if $\lambda = 0$ and $r_\lambda = 0$ if $\lambda \neq 0$, while on the lattice we generically have $0 < r_\lambda < 1$. However, r_λ can be used as a figure of merit to identify WBZMs. In figure 2 on the right we report a scatter plot of r_λ against $|\lambda|/m_s$ for the first

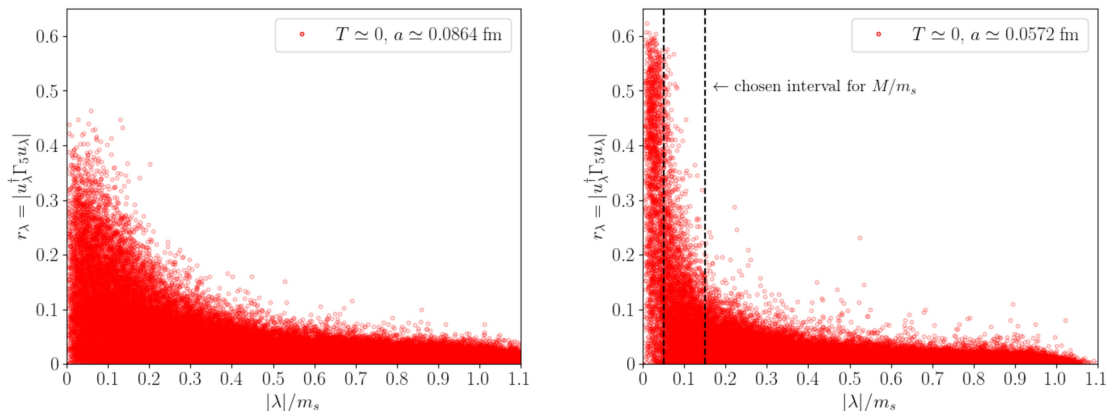


Figure 2. Left: scatter plot of chirality r_λ vs $|\lambda|/m_s$ for a 32^4 lattice with lattice spacing $a = 0.0824$ fm. Only the first 200 eigenvalues (with the lowest magnitude) of 670 configurations (taken every 30 RHMC steps) are shown. Right: scatter plot of chirality r_λ vs $|\lambda|/m_s$ for a 48^4 lattice with lattice spacing $a = 0.0572$ fm. The two dashed vertical lines are set at 0.05 and 0.15 and denote our choice for the M -range. Only the first 200 eigenvalues (with the lowest magnitude) of 540 configurations (taken every 30 RHMC steps) are shown.

200 low-lying modes of 540 $T \approx 0$ configurations (taken every 30 RHMC steps) generated for our finest lattice spacing at this temperature, $a \simeq 0.0572$ fm. It is evident that a sharp separation between WBZMs and non-chiral modes does not exist.

Having seen that the golden strategy is unfeasible, we identified at the finest lattice spacing a range of cut-offs M/m_s chosen to reasonably include in the spectral sums all the modes $|\lambda| \leq M$ that look “chiral enough”; in the following we will simply refer to this range as the “ M -range”. Continuum extrapolation is then performed for several values of M/m_s chosen within this range, and the residual variability will be taken as a systematic of the extrapolation procedure.

The identification of the M -range has been done for the finest lattice spacing because, being the closest point to the continuum limit, the distinction between chiral and non-chiral mode is clearer. For comparison, in figure 2 on the left we also report the scatter plot of r_λ against $|\lambda|/m_s$ for our intermediate lattice spacing at this temperature, $a \simeq 0.0824$ fm. While in this case the identification of a reasonable range for the cut-off appears difficult, for the finest lattice spacing it is clear that for $|\lambda|/m_s \approx 0.1$ there is a change of regime. Therefore, we chose as the M -range the interval $[0.05, 0.15]$.

Once the M -range has been determined, it is possible to extract the continuum limit at fixed value of M/m_s . In figure 3, we compare the continuum limit obtained using the standard gluonic definition with those obtained through SP for two different values of M/m_s . In all cases continuum extrapolation is performed in two different ways: a linear fit in a^2 restricted to the three smallest lattice spacings, and a quadratic fit in a^2 in the whole range, cf. eq. (2.16). Results obtained varying the fit range and the fit function appear to be in very good agreement in all cases, but we observe that SP continuum extrapolations are less sensitive to the fitting procedure adopted, cf. figure 3.

As a matter of fact, if we compare the magnitude of the $O(a^2)$ lattice artifacts affecting the two discretizations, we observe that SP estimates have a much faster convergence

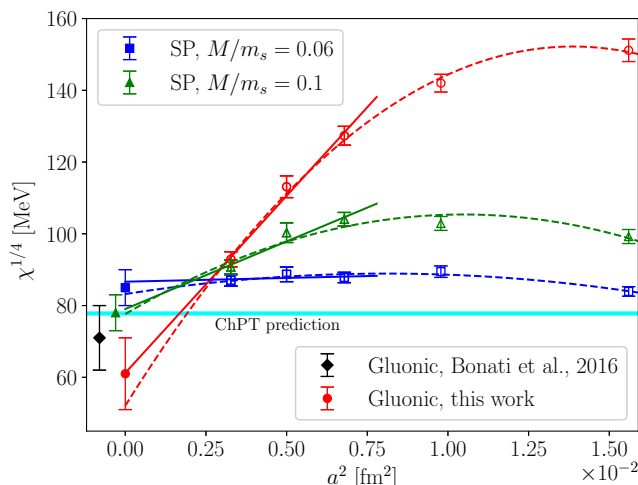


Figure 3. Extrapolation towards the continuum limit of $\chi^{1/4}$ for $T \approx 0$. The horizontal band shows NLO ChPT prediction in eq. (3.1). Our gluonic determinations have been determined through the alpha-rounded clover definition computed on cooled configurations after $n_{\text{cool}} = 100$ cooling steps. The diamond full point represents the gluonic determination reported in ref. [1].

towards the continuum limit. If we denote by c_{SP} the coefficient of the $O(a^2)$ correction to χ for the SP approach (see eq. (2.16)) and by c_{gluo} the corresponding coefficient for the gluonic definition, we have $c_{\text{SP}}(0.06)/c_{\text{gluo}} \sim 10^{-2}$ and $c_{\text{SP}}(0.1)/c_{\text{gluo}} \sim 0.3$ for the two particular values of M/m_s shown in figure 3.

In order to give a final result for $\chi^{1/4}$ from SP, it is necessary to correctly assess the systematic error related to the choice of M/m_s . In figure 4 on the left we show how the SP continuum extrapolation obtained from a linear fit in a^2 of the three finest lattice spacings depends on the choice of $M/m_s \in [0.05, 0.15]$. These determinations are all compatible among each other, however, we observe that, as M/m_s grows, the central value of the continuum extrapolation tends to drift downward. For this reason, our final result $\chi_{\text{SP}}^{1/4} = 80(10)$ MeV is obtained by choosing a confidence interval that keeps this systematic variation into account, cf. figure 4. As for the gluonic result, instead, we estimated the final error from the systematic variation of the extrapolation when changing the fit function and the fit range. These final results are in good agreement among themselves and also with the gluonic determination reported in ref. [1] and with the ChPT prediction in eq. (3.1), as shown in figure 4.

To test the solidity of our results, we performed a further consistency check of our continuum extrapolation procedure, consisting of a common continuum extrapolation of the gluonic results and the SP determinations at fixed M . In this case it is important to include $O(a^4)$ corrections to the gluonic determination and, since SP data show milder lattice artifacts with respect to the gluonic ones, the final result turns out to be practically indistinguishable from the SP continuum extrapolation at the same M value. This test constitutes a non-trivial consistency check of the adopted procedure, and we report as our final estimate

$$\chi_{\text{SP}}^{1/4}(T = 0) = 80(10) \text{ MeV}. \tag{3.2}$$

The same procedure to assess the final error on $\chi^{1/4}$ will also be applied at finite temperature.

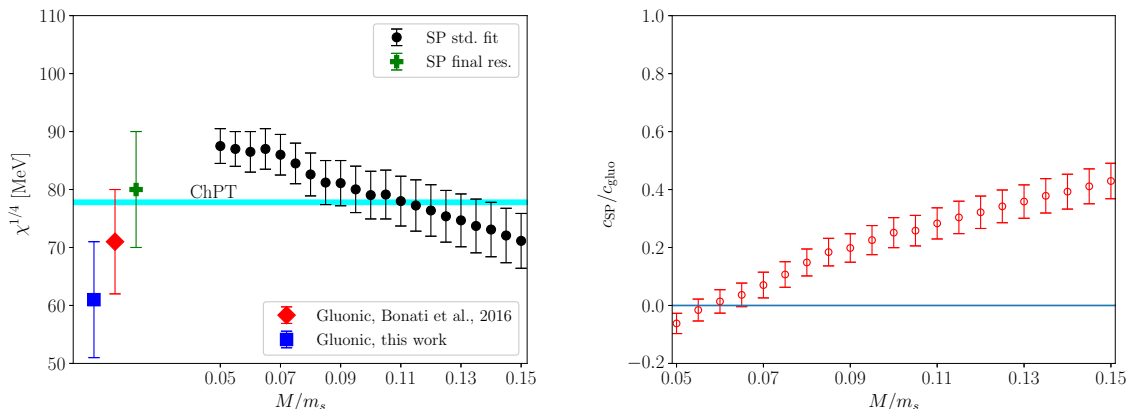


Figure 4. Left: continuum limits of $\chi^{1/4}$ obtained at $T \approx 0$ from spectral projectors for several values of the cut-off M/m_s chosen within the M -range. Each error bar refers to the continuum extrapolation obtained fitting the three finest lattice spacings with the fit function reported in eq. (2.16). The cross point represents our final SP determination of $\chi^{1/4}$, which includes any residual systematic related to the choice of M/m_s . The diamond full point represents the gluonic determination reported in ref. [1]. The horizontal band displays the NLO ChPT result of eq. (3.1). Right: behavior of c_{SP}/c_{gluo} as a function of the cut-off M/m_s within the M -range. A straight horizontal line is set at 0.

Finally, we show in the right plot of figure 4 the dependence of c_{SP}/c_{gluo} on the cut-off M/m_s within the M -range. We observe that the SP discretization is affected by smaller lattice artifacts compared to the gluonic definition, and that corrections to the continuum limit grow as M/m_s is increased, getting closer to those of the gluonic discretization. This is due to the fact that, as M/m_s grows, the number of irrelevant non-chiral modes, which are more affected by UV cut-off effects, included in the spectral sums grows too.

3.2 Topological susceptibility at finite temperature

We computed the topological susceptibility for five temperature values in the high temperature phase of QCD, and specifically for $T \simeq 230$ MeV, $T \simeq 300$ MeV, $T \simeq 365$ MeV, $T \simeq 430$ MeV and $T \simeq 570$ MeV. In this section, we will discuss the details of the $T = 430$ MeV case; a similar analysis has been carried out also for the other temperature values, and the results obtained in these cases are reported in appendix A.

Simulations at $T \simeq 430$ MeV have been performed on $N_s^3 \times N_t$ lattices following the same LCP already used in the zero temperature case; simulation parameters are reported in table 2. The spatial extent of the lattice was chosen to ensure an aspect ratio not smaller than 3.

Simulations at finite temperature, unlike those at $T = 0$, have been performed adopting the multicanonical algorithm. Our implementation of the multicanonical algorithm closely follows the one already adopted in ref. [5]. The quantity Q_{mc} entering the topological potential is the clover discretization (2.4) of the topological charge computed after n_{mc} levels of stout smearing, which allows to adopt the RHMC algorithm also in the presence of the topological potential. The values of n_{mc} used ranged from $n_{mc} = 20$ for the coarsest

β	a [fm]	$\hat{m}_s \cdot 10^{-2}$	N_s	N_t
4.140	0.0572	2.24	32	8
4.280	0.0458	1.81	32	10
4.385	0.0381	1.53	36	12
4.496	0.0327	1.29	48	14
4.592	0.0286	1.09	48	16

Table 2. Simulation parameters for the runs at $T = 1/(aN_t) \simeq 430$ MeV $\simeq 2.8 T_c$. The bare parameters β , \hat{m}_s and the lattice spacings have been fixed according to the LCP determined in refs. [38–40], and \hat{m}_l is fixed through $\hat{m}_s/\hat{m}_l = m_s/m_l = 28.15$.

lattice spacing to $n_{\text{mc}} = 10$ for the finest one, while the isotropic smearing parameter was always fixed to $\rho_{\text{mc}} = 0.1$. The functional form of the topological potential adopted was [5]:

$$V_{\text{topo}}(x) = \begin{cases} -\sqrt{(Bx)^2 + C}, & |x| < Q_{\text{max}}, \\ -\sqrt{(BQ_{\text{max}})^2 + C}, & |x| \geq Q_{\text{max}}, \end{cases} \quad (3.3)$$

and in our simulations, $Q_{\text{max}} = 3$ turned out to be sufficient to observe a dramatic enhancement in the number of fluctuations of Q_{gluo} . The free parameters B and C have instead been tuned through short preliminary runs by requiring the Monte Carlo histories of the measured topological charge Q_{gluo} to uniformly explore the interval $[-Q_{\text{max}}, Q_{\text{max}}]$.

The improvement obtained with the multicanonic algorithm is exemplified in figure 5. Without any bias potential, Q_{gluo} assumes a non-zero value only a handful of times, while much more fluctuations are observed as the topological potential is switched on.³ This allows to dramatically improve the accuracy with which χ can be computed with a given machine time budget.

In order to compute the topological susceptibility, we follow the same procedure already discussed for the $T \simeq 0$ case in section 3.1. The first step consists of determining a reasonable interval for M/m_s by studying the scatter plot of the chiralities for the finest lattice spacing available, which is shown in figure 6 on the right.

With respect to the $T \simeq 0$ case, at finite temperature the separation between high and low-chirality modes is more evident, as two almost disconnected clusters can be observed with $r_\lambda \sim 0.7 - 0.8$ and $r_\lambda \lesssim 0.5$. However, also in this case, the isolation of WBZMs is an ambiguous task, as we also observe a sparsely-populated group of modes in between, with $0.5 \lesssim r_\lambda \lesssim 0.7$.

Such an ambiguity is not a characteristic of the whole configuration ensemble, but already arises configuration by configuration. In figure 7, we plot the histogram of the separation between candidate WBZMs and Non-Zero Modes (NZMs) for the same sample represented in the scatter plot of figure 6 on the right.

The candidate WBZMs were identified from the value of the gluonic topological charge: more precisely we assumed the first $n_t|Q_{\text{gluo}}|$ lowest-lying eigenmodes of iD_{stag} to be the WBZMs (the factor $n_t = 4$ takes into account the four tastes of staggered fermions). This

³In ref. [5] it has been checked, whenever a simulation without multicanonic algorithm was feasible too, that the adoption of the multicanonic algorithm does not introduce any bias and yields the same result for topological observables.

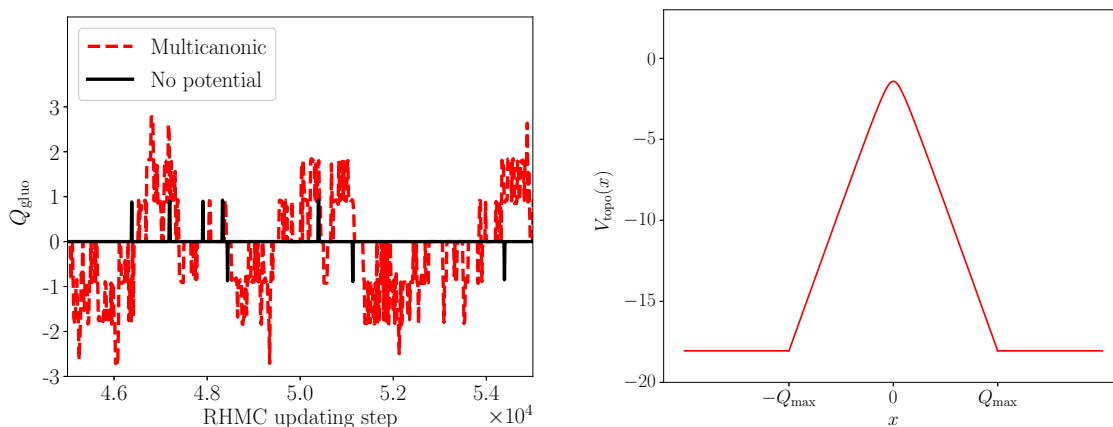


Figure 5. Left: comparison between the Monte Carlo histories of Q_{gluo} obtained with and without bias potential for our run with $\beta = 4.140$ at $T \simeq 430$ MeV. Since for this point one RHMC step in the presence of the potential requires a $\sim 60\%$ larger numerical effort, to make the comparison fair we expressed the Monte Carlo time on the horizontal axis in units of one standard RHMC step in both cases. Right: functional form (3.3) of the bias potential. In this case $B = 6$, $C = 2$ and $Q_{\text{max}} = 3$.

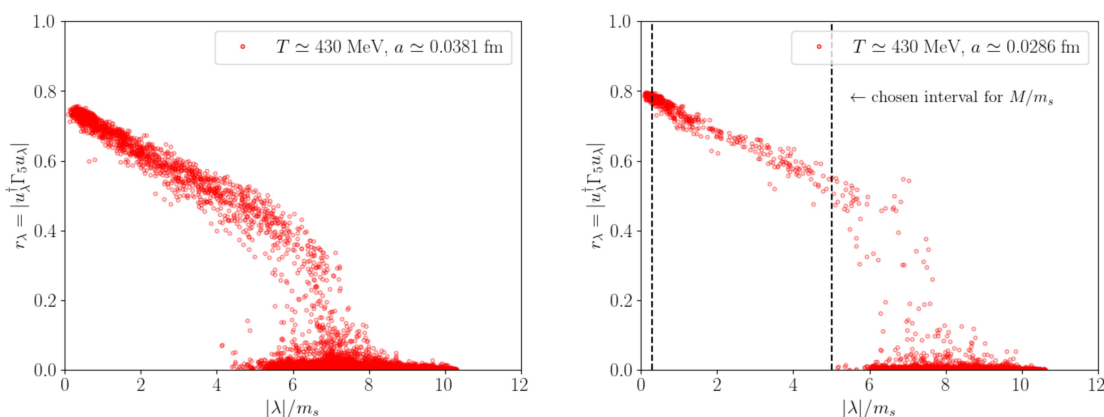


Figure 6. Left: scatter plot of the chirality r_λ vs $|\lambda|/m_s$ for our run with $a \simeq 0.0381$ fm at $T \simeq 430$ MeV. Only the first 200 eigenvalues (with the lowest magnitude) of 227 configurations (taken every 30 RHMC steps) are shown. Right: scatter plot of the chirality r_λ vs $|\lambda|/m_s$ for our run with $a \simeq 0.0286$ fm at $T \simeq 430$ MeV. The two dashed vertical lines are set at 0.3 and 5 and delimit the chosen M -range. Only the first 200 eigenvalues (with the lowest magnitude) of 184 configurations (taken every 1200 RHMC steps) are shown.

strategy is the same adopted in ref. [3] to identify WBZMs for their reweighting procedure, and it is justified on the basis of the index theorem for staggered fermions in the continuum $n_t Q = n_+ - n_-$, supplemented by the assumption that $n_- = 0$ ($n_+ = 0$) if $Q > 0$ ($Q < 0$), which should be approximately true if the lattice volume is not too large. However, we observe that the typical relative separation between WBZMs and NZMs is of the order of $10^{-2} \div 10^{-1}$, cf. figure 7, meaning that a sharp separation between WBZMs and NZMs cannot be unambiguously established already at the level of the single configuration.

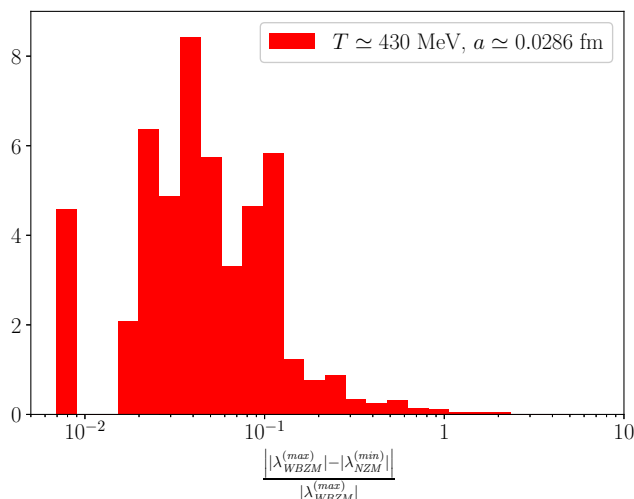


Figure 7. Histogram of the absolute value of the relative separation between the magnitude of the largest eigenvalue of the candidate WBZMs $|\lambda_{WBZM}^{(max)}|$ and the smallest eigenvalue of the candidate NZMs $|\lambda_{NZM}^{(min)}|$. The identification of WBZMs was tentatively obtained, configuration by configuration, considering the first smallest $n_t|Q_{gluo}|$ eigenvalues of iD_{stag} . The plot refers to the finest lattice spacing $a \simeq 0.0286$ fm explored at $T \simeq 430$ MeV.

Thus, we cautiously choose our cut-off masses in the interval $M/m_s \in [0.3, 5]$ in order to include in our spectral sums all modes with $|\lambda| \leq M$ and $r_\lambda \gtrsim 0.5$. Again, the M -range has been identified for the finest lattice spacing available at this temperature, $a \simeq 0.0286$ fm. However, we observe that at finite temperature also intermediate lattice spacings would lead approximately to the same choice. For comparison, in figure 6 on the left, we also report the scatter plot of r_λ against $|\lambda|/m_s$ for an intermediate lattice spacing at this temperature, $a \simeq 0.0381$ fm.

In figure 8 we compare results for $\chi_{SP}^{1/4}$ at $a \simeq 0.0572$ fm obtained, respectively, by computing the multiplicative renormalization constant $Z_{SP}^{(stag)}$ in eq. (2.13) from our finite temperature ensemble generated on a $32^3 \times 8$ lattice and from a corresponding zero temperature ensemble on a 32^4 lattice. We recall that, while the computation of the spectral traces appearing in the definition of $Q_{SP,bare}^{(stag)}$ in eq. (2.11) has been done from the staggered spectrum of D_{stag} where anti-periodic boundaries are imposed along the temporal direction, the computation of $Z_{SP}^{(stag)}$ in eq. (2.13) is done from the staggered spectrum in the presence of periodic boundaries. While this choice matters at finite temperature, it is irrelevant at zero temperature.

As figure 8 shows, both ways of computing $\chi_{SP}^{1/4}$ give perfectly consistent results, in agreement with results obtained at finite temperature in the quenched theory [32]. For this reason, for all lattice spacings we computed both $Z_{SP}^{(stag)}$ and $Q_{SP}^{(stag)}$ from our finite temperature ensembles, where the staggered spectrum entering the spectral definition of these quantities was obtained, respectively, imposing periodic and anti-periodic boundaries along the time direction for D_{stag} .

In figure 9, we compare the continuum limits of $\chi^{1/4}$ obtained via the gluonic and the SP definitions, using the same fit function in eq. (2.16) already adopted for the $T = 0$

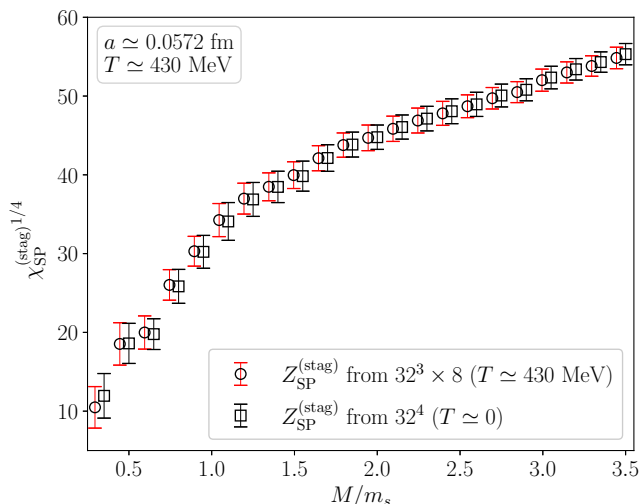


Figure 8. Comparison of $\chi_{\text{SP}}^{(\text{stag})1/4}$ as a function of M/m_s for $a \simeq 0.0572$ fm and at $T \simeq 430$ MeV when the multiplicative renormalization constant $Z_{\text{SP}}^{(\text{stag})}$ is computed on our finite temperature ensemble (on a $32^3 \times 8$ lattice) or on a corresponding zero-temperature ensemble (on a 32^4 lattice). The quantity $Z_{\text{SP}}^{(\text{stag})}$ was computed in both cases using the staggered spectrum obtained imposing periodic boundaries along the temporal direction for D_{stag} .

case. For the SP case, we show results for the values $M/m_s = 0.3$ and 0.5 . As for the zero-temperature case, also at finite temperature we observe that the SP definition allows to achieve a sensible reduction of the magnitude of $O(a^2)$ corrections with respect to the gluonic case, $c_{\text{SP}}(0.3)/c_{\text{gluo}} \sim 5 \times 10^{-2}$ and $c_{\text{SP}}(0.5)/c_{\text{gluo}} \sim 10^{-1}$, allowing for a better control over systematics related to the continuum extrapolation, as we observe a very good agreement in the obtained extrapolations when varying the fit range and the fit function. Moreover, we observe a good agreement among the gluonic and the SP determinations, cf. figure 9.

Finally, in figure 10, we show how the continuum limit of χ_{SP} varies as a function of M/m_s within the M -range interval determined before (left plot). Also at finite temperature we observe that the continuum limit of $\chi_{\text{SP}}^{1/4}$ is quite stable within the M -range; nevertheless the residual systematic is incorporated in our final result, also shown in figure 10. As for the gluonic case, the final error was instead estimated from the systematic variation of the continuum extrapolation varying the fit function and the fit range, similarly to the procedure followed at zero temperature. Finally, we also checked that performing a common fit to our gluonic results and our SP determinations for a fixed value of M/m_s gave consistent results with the extrapolations performed for the SP determinations alone at the same value of M/m_s . As already done at zero temperature, we consider the conservative estimate $\chi_{\text{SP}}^{1/4} = 15(5)$ MeV as our final determination, where this error takes into account both the systematic and the statistical sources of uncertainty.

In figure 10, in the right plot, we also report how the ratio $c_{\text{SP}}/c_{\text{gluo}}$ depends on M/m_s . As already observed when discussing the $T = 0$ results, when M/m_s is chosen small enough,

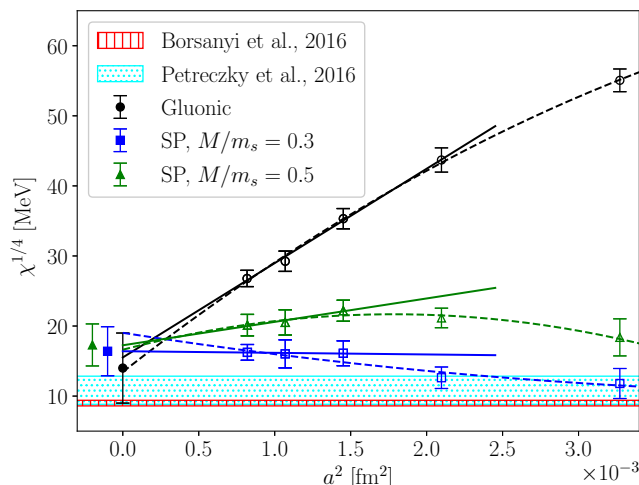


Figure 9. Comparison of the continuum limits of $\chi^{1/4}$ for $T \simeq 430$ MeV obtained with the gluonic and the SP discretizations. Vertically-hatched and dotted-hatched bands display the values of $\chi^{1/4}$ obtained for this temperature in, respectively, refs. [3, 4]. The former was temperature-interpolated according to the DIGA prediction $\chi^{1/4} \sim T^{-2}$ and the isospin-breaking factor was removed. The latter was mass-extrapolated according to $\chi^{1/4} \sim m_\pi$.

the SP discretization suffers for much smaller lattice artifacts compared to the gluonic one. As this cut-off increases, the ratio $c_{\text{SP}}/c_{\text{gluo}}$ tends to grow, approaching 1, which can be interpreted as the effect of the inclusion of more and more non-chiral modes in the spectral sums.

We now want to compare our final SP result for $\chi^{1/4}$ at $T \simeq 430$ MeV, $\chi^{1/4} = 15(5)$ MeV, with other determinations at this temperature. This value is compatible with our gluonic estimation ($\chi^{1/4} = 14(5)$ MeV) and is also compatible within $\sim 1.2\sigma$ with the value that can be obtained interpolating results of ref. [3] in table S9 according to the DIGA prediction $\chi^{1/4} \sim T^{-2}$ and removing the isospin-breaking factor 0.88 the authors use to restore the $u-d$ mass difference in their $N_f = 2 + 1 + 1$ results for the susceptibility: $\chi^{1/4} = 9.0(4)$ MeV. Our determination is also in agreement within the errors with the gluonic result reported in ref. [4] for this temperature: $\chi^{1/4} = 11(2)$ MeV. Note however that in this case the comparison is less strict as the latter result was obtained rescaling gluonic determinations for $\chi^{1/4}$ reported in ref. [4] by $(135 \text{ MeV})/m_\pi$, as they were obtained for $m_\pi \approx 160$ MeV. Of course this procedure assumes that χ depends on the light quark mass as predicted by the DIGA: $\chi^{1/4} \sim m_l^{1/2} \sim m_\pi$. Finally, we mention that in ref. [4] the authors also computed $\chi^{1/4}$ adopting a fermionic definition based on the disconnected chiral susceptibility, which was however fully consistent with the gluonic results used above.

3.3 $\chi(T)$ from spectral projectors and comparison with the DIGA

In our $N_f = 2 + 1$ setup, semiclassical and perturbative approximations predict for the topological susceptibility when $T \gg T_c$ the scaling (see eq. (1.2))

$$\chi^{1/4}(T) \propto T^{-b}, \quad b_{\text{DIGA}} = 2. \quad (3.4)$$

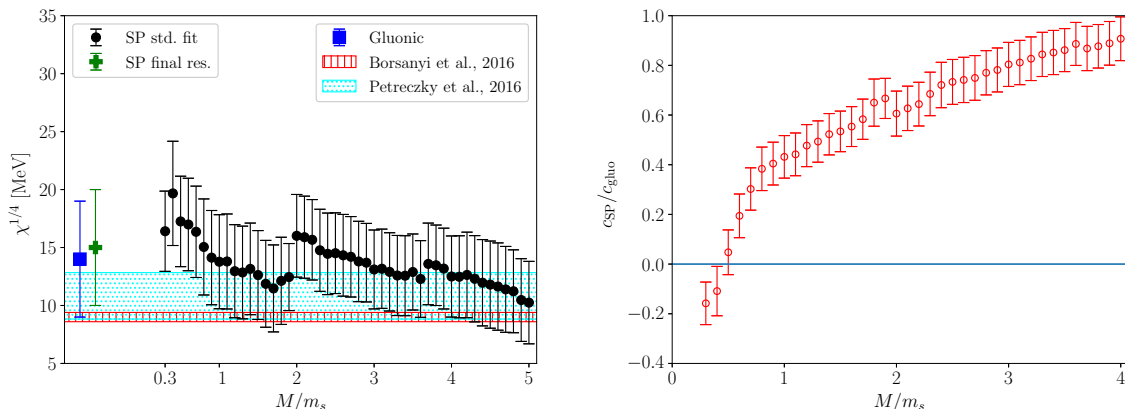


Figure 10. Left: continuum limits of $\chi^{1/4}$ obtained at $T \simeq 430$ MeV from spectral projectors for several values of the cut-off M/m_s within the M -range. Each error bar refers to the continuum extrapolation obtained fitting the three finest lattice spacings with the fit function reported in eq. (2.16). The cross point represents our final SP determination of $\chi^{1/4}$, which includes any residual systematic related to the choice of M/m_s . Vertically-hatched and dotted-hatched bands display the values of $\chi^{1/4}$ obtained for this temperature in, respectively, refs. [3, 4]. The former was temperature-interpolated according to the DIGA prediction $\chi^{1/4} \sim T^{-2}$ and the isospin-breaking factor was removed. The latter was mass-extrapolated according to $\chi^{1/4} \sim m_\pi$. Right: behavior of $c_{\text{SP}}/c_{\text{gluo}}$ as a function of M/m_s within the M -range. A straight horizontal line is set at 0.

T [MeV]	T/T_c	$\chi_{\text{SP}}^{1/4}$ [MeV]	$\chi_{\text{gluo}}^{1/4}$ [MeV]
230	1.48	49(11)	38(8)
300	1.94	41(8)	32(10)
365	2.35	26.5(5.5)	20(7)
430	2.77	15(5)	14(5)
570	3.68	8(6)	6(6)

Table 3. Results for the fourth root of the topological susceptibility as a function of T . For the crossover temperature T_c we adopted the reference value $T_c = 155$ MeV.

The aim of the present section is to study the behavior of our results for $\chi^{1/4}$ as a function of T and to compare it with the DIGA prediction. Our final results for $\chi^{1/4}$ as a function of T/T_c , obtained both from the gluonic and the SP definitions, are reported in table 3. These results were obtained following exactly the same strategy outlined in section 3.2 for $T \simeq 430$ MeV, and more details about them can be found in appendix A.

In figure 11, we show the behavior of $\chi^{1/4}$ as a function of T/T_c , from which it should be clear that our data are compatible with a power-law behavior of the type (3.4) in the whole explored range. If we perform a best fit of the data using the function

$$\chi^{1/4} = A \left(\frac{T}{T_c} \right)^{-b} \tag{3.5}$$

when including in the fit all available points, we obtain the results

$$b_{\text{SP}} = 1.82(43), \quad b_{\text{gluo}} = 1.67(51).$$

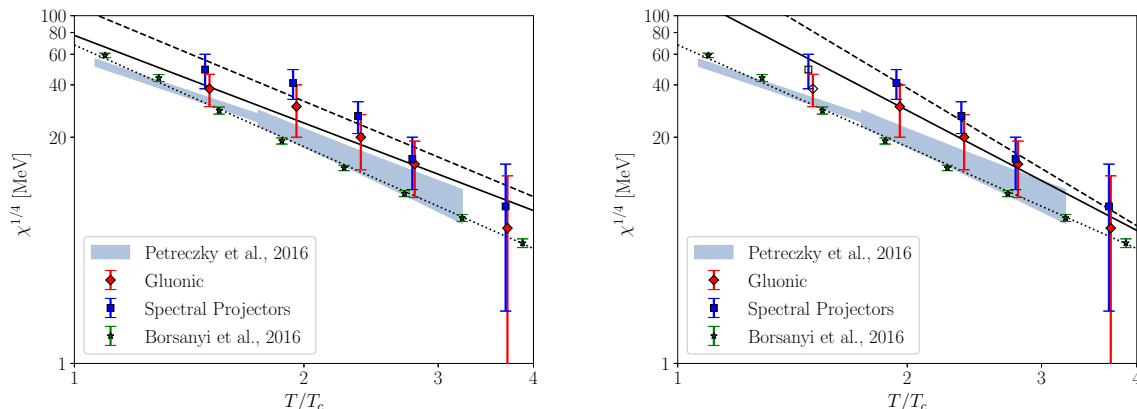


Figure 11. Behavior of $\chi^{1/4}$ as a function of T/T_c in double-log scale for our SP and gluonic data. Gluonic points are slightly shifted to improve readability. Starred points represent results taken from ref. [3], where the isospin-breaking factor was removed, while the uniform-shaded area represents the gluonic determinations reported in ref. [4], which have been mass-rescaled according to $\chi^{1/4} \sim m_\pi$. The left plot reports the best fits of our data according to the fit function (3.5) and performed including all available points: $\tilde{\chi}^2/\text{dof} = 0.54/3$ for gluonic data and $\tilde{\chi}^2/\text{dof} = 2.1/3$ for SP ones. The right plot reports the result of the same fits, but performed excluding our lowest temperature $T \simeq 230$ MeV (excluded points are empty). In this case, $\tilde{\chi}^2/\text{dof} = 0.06/2$ for gluonic data and $\tilde{\chi}^2/\text{dof} = 0.22/2$ for SP ones. Dashed, solid and dotted lines represent, respectively, best fits of our gluonic data, of our spectral data and of gluonic data of ref. [3].

If we instead exclude from the fit the lowest temperature $T = 230$ MeV, we get:

$$b_{\text{SP}} = 2.63(81), \quad b_{\text{gluo}} = 2.3(1.1).$$

We thus conclude that our data are in perfect agreement with a power-law behavior in the whole explored range, with an effective exponent that turns out to be well compatible with b_{DIGA} within our errors already for $T \gtrsim 300$ MeV, i.e., already for $T/T_c \gtrsim 2$. Actually, also when $T = 230$ MeV is included in the fit the exponent b_{SP} turns out to be compatible within 1 standard deviation with b_{DIGA} . However, as it can be clearly seen from figures 11, the inclusion/exclusion of such point visibly changes the slope of the fit. This may be an indication, albeit at present not conclusive, that the effective exponent b changes when going from $T \sim 200$ MeV to $T \sim 300$ MeV.

In figure 11 we also compare our results with previous determinations reported in refs. [3, 4]. Concerning results of ref. [3], to make a fair comparison, we removed the isospin-breaking factor the authors use to restore the $u - d$ mass difference in their $N_f = 2 + 1 + 1$ results. Our spectral determinations are systematically larger than those of ref. [3], and we find a $\sim 2.5 - 3$ standard deviation tension at $T = 300$ MeV and $T = 365$ MeV. As for the temperature behavior, we observe that the best fit of the data of ref. [3] for $T \gtrsim 170$ MeV with the fit function (3.5) yields $b = 1.945(23)$, i.e., in this case the DIGA-like power-law seems to set in for smaller values of the temperature.

Concerning the gluonic results of ref. [4], since they were obtained for $m_\pi = 160$ MeV, we rescaled them according to the DIGA prediction $\chi^{1/4} \sim m_\pi$ in order to make a fair comparison. Also in this case we observe that our determinations lay systematically above.

Although this comparison is less strict because of the different pion masses adopted, also in this case we observe a $\sim 2 - 2.5$ standard deviation tension among determinations for $T = 300$ MeV and $T = 365$ MeV.

The observed tensions between our spectral determinations and previous results reported in the literature deserve to be further investigated, for example by refining the present errors on the spectral determinations for $T \lesssim 400$ MeV. Also probing higher temperatures with our methods would be interesting in order to extend the present comparison towards the ~ 1 GeV region, which is also interesting in the context of axion cosmology.

4 Conclusions

In this work we performed a numerical lattice study of the behavior of the topological susceptibility $\chi(T)$ in the high temperature regime of QCD with $N_f = 2 + 1$ quarks at the physical point.

Our computational strategy relies on the discretization of the topological charge through Spectral Projectors on the eigenmodes of the staggered Dirac operator. The reason for this choice is to reduce the large lattice artifacts affecting the gluonic definition of χ at high temperatures when non-chiral quarks, like the staggered ones, are adopted to discretize the QCD action. The problem of the dominance of the $Q = 0$ sector, which is related to the suppression of χ at high- T , is instead addressed by the use of the multicanonical method already applied for this purpose in the recent work [5].

The spectral definition of the topological susceptibility introduces a new free parameter, as the sum over the chiralities of the eigenmodes of the lattice staggered Dirac operator is performed by including all eigenvalues with magnitude $|\lambda| \leq M$. In principle, any value of M (kept constant in physical units as $a \rightarrow 0$) would provide a correct continuum limit of χ ; however, since isolating WBZMs is highly ambiguous, we identified a reasonable range of M -values on which to perform the continuum limit at fixed M . Any residual systematic related to the choice of M is then assessed afterwards and included in our final determination of the uncertainty affecting χ .

To test the spectral method we first of all study the $T = 0$ case, where χ can be reliably computed by using chiral perturbation theory. In this case the multicanonical algorithm is not needed, since the MC evolution naturally visits $Q \neq 0$ sectors, and the final result obtained by the spectral method is perfectly compatible both with the NLO ChPT result and with previous gluonic estimates.

The advantage of the spectral projectors method with respect to the gluonic one is that lattice artifacts are in this case much smaller, and the extrapolation towards the continuum limit is thus better under control. Moreover, due to the presence of the parameter M , in the spectral projectors setting we have a natural procedure to check for the presence of systematics in the continuum extrapolation procedure: to look for residual dependence on M of the extrapolated result. As a matter of fact, this systematic gives the dominant contribution to the final error on χ for some of the temperatures studied in this work.

In the high temperature regime, we explored 5 values of T , ranging from ~ 200 MeV to ~ 600 MeV. Also in these cases we observe good agreement between SP and gluonic data,

with the spectral results that are generically more accurate than the gluonic ones; however, more important is that, as noted above, in the SP case we have a much better control of the systematics of the continuum extrapolation.

We finally investigated the behavior of our results for χ as a function of T , comparing with expectations based on the DIGA approximation. We find that a decaying power law well describes our data in the whole explored range; in particular the effective exponent of this power law is well in agreement with the DIGA prediction for $T \gtrsim 300$ MeV, i.e., for $T/T_c \gtrsim 2$. This is in agreement with the results obtained in ref. [4] and is consistent with a growing number of observations suggesting that high-temperature QCD is dominated by strong non-perturbative effects for temperatures going approximately from the chiral crossover up to ~ 300 MeV [66–69].

We remark that our results for $\chi^{1/4}$ from spectral projectors show a $\sim 2 - 3$ standard deviation tension in the range $300 \text{ MeV} \lesssim T \lesssim 400 \text{ MeV}$ range when compared with previous determinations in refs. [3, 4]. Moreover, also when the consistency between our results and the ones in the literature is better, our spectral determinations for $\chi^{1/4}(T)$ systematically points to larger values in the whole explored range. The same behavior, when observed in the gluonic determinations of χ , could be ascribed to a problem of the continuum extrapolation, that is unable to capture the asymptotic $O(a^2)$ scaling and introduces a bias in the extrapolation. The lattice spacing dependence of the SP determinations is however much milder than that of the gluonic estimates, and such an interpretation of the observed disagreement seems unlikely in this case. In conclusion, the picture emerging from the comparison carried out in figure 11 is that a complete quantitative understanding of the behavior of $\chi(T)$ in the high temperature regime of QCD is still missing, and further studies will be required to clarify the sources of the observed tensions between different determinations.

Several directions can be followed to improve the present study: first of all it seems crucial to refine our present estimates of the topological susceptibility, in order to make the comparison with the results of refs. [3, 4] more stringent, and obtain a precise and unbiased estimate of $\chi(T)$ in the explored temperature range. For this purpose simulations with larger statistics and smaller lattice spacings are required. Other natural extensions include a systematic study of the temperature ranges $T \lesssim 400$ MeV, where deviations from the DIGA power law should be visible, and $T \sim 1$ GeV, in order to reach the region of temperatures directly relevant for axion cosmology.

However, simulations at smaller lattice spacings (needed both to improve the present estimates and to reach higher temperatures) are practically unfeasible with standard RHMC simulations, due to the severe topological critical slowing down. A promising strategy to overcome this problem is the *parallel tempering on boundary conditions* algorithm proposed in ref. [70], which has already been successfully applied both to two dimensional models [70, 71] and to $4d$ $SU(N)$ Yang-Mills theories without matter fields [72, 73].

Acknowledgments

A. A. has been financially supported by the European Union’s Horizon 2020 research and innovation programme “Tips in SCQFT” under the Marie Skłodowska-Curie grant

T [MeV]	T/T_c	β	a [fm]	$\hat{m}_s \cdot 10^{-2}$	N_s	N_t
230	1.48	3.814	0.1073	4.27	32	8
		3.918	0.0857	3.43	40	10
		4.014	0.0715	2.83	48	12
		4.100	0.0613	2.40	56	14
		4.181	0.0536	2.10	64	16
300	1.94	3.938	0.0824	3.30	32	8
		4.059	0.0659	2.60	40	10
		4.165	0.0549	2.15	48	12
		4.263	0.0470	1.86	56	14
365	2.35	4.045	0.0676	2.66	32	8
		4.175	0.0541	2.12	40	10
		4.288	0.0451	1.78	48	12
		4.377	0.0386	1.55	56	14
570	3.68	4.140	0.0572	2.24	24	6
		4.316	0.0429	1.71	32	8
		4.459	0.0343	1.37	40	10
		4.592	0.0286	1.09	48	12

Table 4. Simulation parameters used for $T \simeq 230$ MeV, $T \simeq 300$ MeV, $T \simeq 365$ MeV and $T \simeq 570$ MeV. The bare parameters β , \hat{m}_s and the lattice spacings have been fixed according to results of refs. [38–40], and \hat{m}_l is fixed through $\hat{m}_s/\hat{m}_l = m_s/m_l = 28.15$.

agreement No. 791122, as well as by the Horizon 2020 European research infrastructures programme “NI4OS-Europe” with grant agreement no. 857645. C. Bonanno acknowledges the support of the Italian Ministry of Education, University and Research under the project PRIN 2017E44HRF, “Low dimensional quantum systems: theory, experiments and simulations”. M. D. thanks Sayantan Sharma for useful discussions. Numerical simulations have been performed on the MARCONI and MARCONI100 machines at CINECA, based on the agreement between INFN and CINECA (under projects INF19_npqcd, INF20_npqcd and INF21_npqcd).

A Summary of finite temperature results for χ

We here report all the results for χ at finite temperature not shown in section 3.2, following the same order of presentation of that section. Each subsection refers to a single temperature and results are shown as follows:

- scatter plot of the chiralities of the lowest eigenmodes of the staggered operator for the finest lattice spacing explored at that temperature;
- comparison of the continuum limits obtained for the gluonic and the SP definitions;
- assessment of the systematics related to the choice of M/m_s .

The parameters of all the performed simulations are summarized in table 4. For the two coarsest lattice spacings simulated at $T = 230$ MeV, no enhancement of topological fluctuations was needed; therefore, simulations of these points were carried on without the multicanonic algorithm.

A.1 $T = 230$ MeV

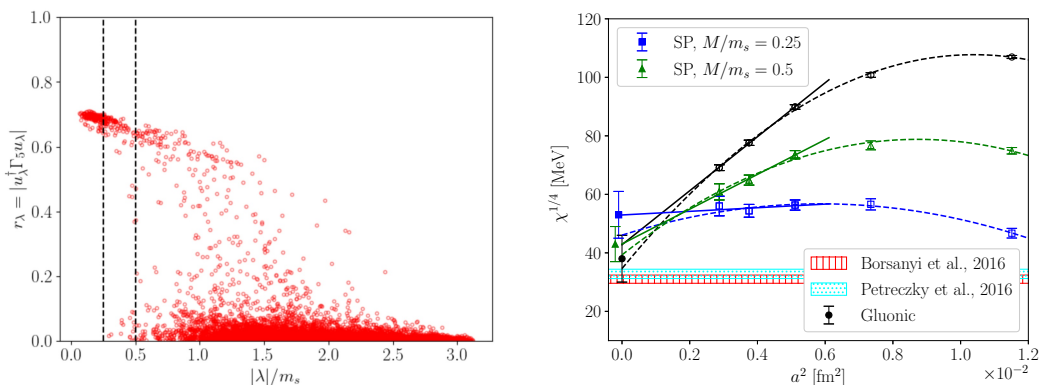


Figure 12. Left: scatter plot of the chirality r_χ vs $|\lambda|/m_s$ for our run with $a \simeq 0.0536$ fm at $T \simeq 230$ MeV. The two dashed vertical lines are set at 0.25 and 0.5 and delimit the chosen interval for M/m_s . For each reported configuration, only the first 200 eigenvalues (with the lowest magnitude) are shown. Right: comparison of the continuum limits of $\chi^{1/4}$ for $T \simeq 230$ MeV obtained with the gluonic and the SP discretizations. Vertically-hatched and dotted-hatched bands display the values of $\chi^{1/4}$ obtained for this temperature in, respectively, refs. [3, 4]. The former was temperature-interpolated according to the DIGA prediction $\chi^{1/4} \sim T^{-2}$ and the isospin-breaking factor was removed. The latter was mass-extrapolated according to $\chi^{1/4} \sim m_\pi$.

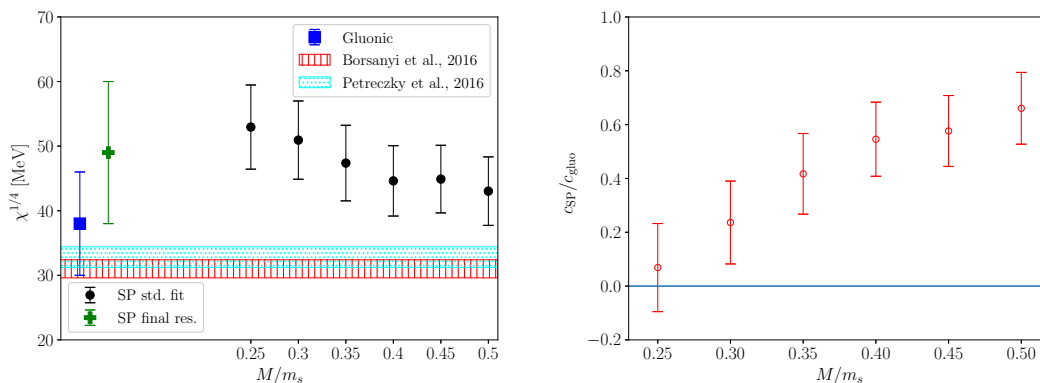


Figure 13. Left: continuum limits of $\chi^{1/4}$ obtained at $T \simeq 230$ MeV from spectral projectors for several values of M/m_s within the M -range. Each error bar refers to the continuum extrapolation obtained fitting the three finest lattice spacings with the fit function reported in eq. (2.16). The cross point is our final SP result, which includes any residual systematic related to the choice of M/m_s . Vertically-hatched and dotted-hatched bands display the values of $\chi^{1/4}$ obtained for this temperature in, respectively, refs. [3, 4]. The former was temperature-interpolated according to the DIGA prediction $\chi^{1/4} \sim T^{-2}$ and the isospin-breaking factor was removed. The latter was mass-extrapolated according to $\chi^{1/4} \sim m_\pi$. Right: c_{SP}/c_{gluo} for the several values of M/m_s within the M -range. A straight horizontal line is set at 0.

A.2 $T = 300$ MeV

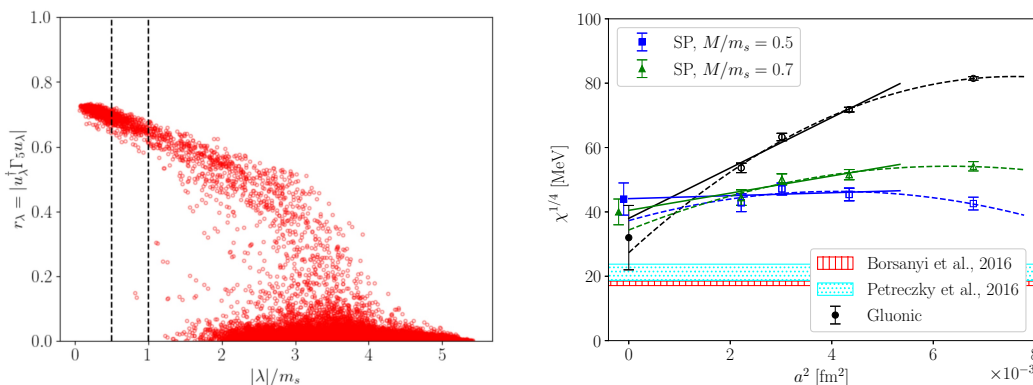


Figure 14. Left: scatter plot of the chirality r_χ vs $|\lambda|/m_s$ for our run with $a \simeq 0.0470$ fm at $T \simeq 300$ MeV. The two dashed vertical lines are set at 0.5 and 1 and delimit the chosen interval for M/m_s . For each reported configuration, only the first 200 eigenvalues (with the lowest magnitude) are shown. Right: comparison of the continuum limits of $\chi^{1/4}$ for $T \simeq 300$ MeV obtained with the gluonic and the SP discretizations. Vertically-hatched and dotted-hatched bands display the values of $\chi^{1/4}$ obtained for this temperature in, respectively, refs. [3, 4]. The former was temperature-interpolated according to the DIGA prediction $\chi^{1/4} \sim T^{-2}$ and the isospin-breaking factor was removed. The latter was mass-extrapolated according to $\chi^{1/4} \sim m_\pi$.

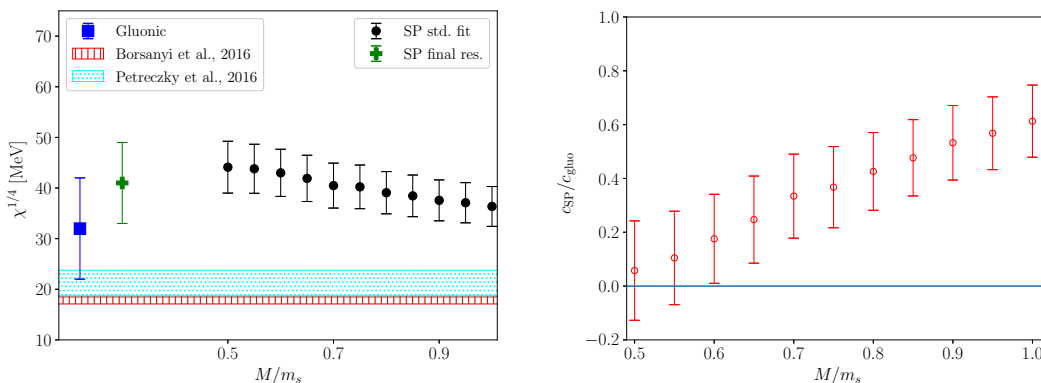


Figure 15. Left: continuum limits of $\chi^{1/4}$ obtained at $T \simeq 300$ MeV from spectral projectors for several values of M/m_s within the M -range. Each error bar refers to the continuum extrapolation obtained fitting the three finest lattice spacings with the fit function reported in eq. (2.16). The cross point is our final SP result, which includes any residual systematic related to the choice of M/m_s . Vertically-hatched and dotted-hatched bands display the values of $\chi^{1/4}$ obtained for this temperature in, respectively, refs. [3, 4]. The former was temperature-interpolated according to the DIGA prediction $\chi^{1/4} \sim T^{-2}$ and the isospin-breaking factor was removed. The latter was mass-extrapolated according to $\chi^{1/4} \sim m_\pi$. Right: c_{SP}/c_{gluo} for the several values of M/m_s within the M -range. A straight horizontal line is set at 0.

A.3 $T = 365$ MeV

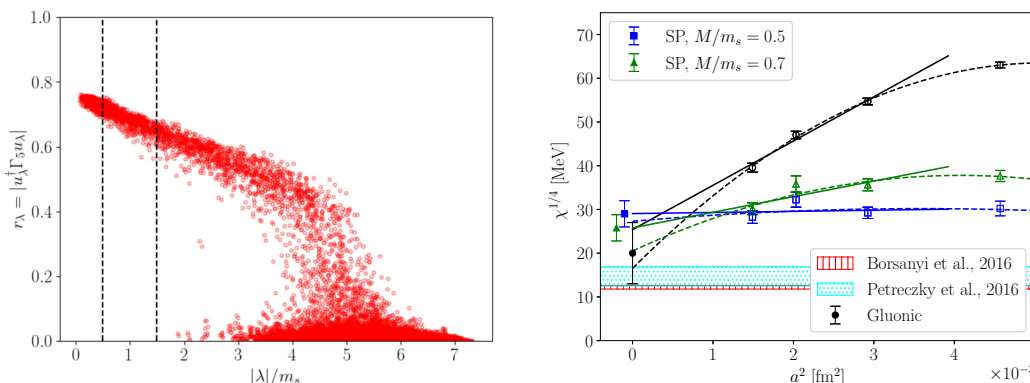


Figure 16. Left: scatter plot of the chirality r_λ vs $|\lambda|/m_s$ for our run with $a \simeq 0.0386$ fm at $T \simeq 365$ MeV. The two dashed vertical lines are set at 0.5 and 1.5 and delimit the chosen interval for M/m_s . For each reported configuration, only the first 200 eigenvalues (with the lowest magnitude) are shown. Right: comparison of the continuum limits of $\chi^{1/4}$ for $T \simeq 365$ MeV obtained with the gluonic and the SP discretizations. Vertically-hatched and dotted-hatched bands display the values of $\chi^{1/4}$ obtained for this temperature in, respectively, refs. [3, 4]. The former was temperature-interpolated according to the DIGA prediction $\chi^{1/4} \sim T^{-2}$ and the isospin-breaking factor was removed. The latter was mass-extrapolated according to $\chi^{1/4} \sim m_\pi$.

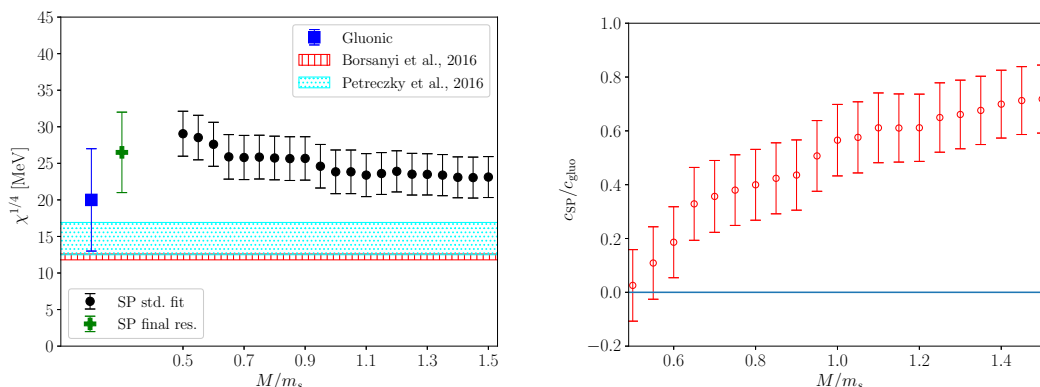


Figure 17. Left: continuum limits of $\chi^{1/4}$ obtained at $T \simeq 365$ MeV from spectral projectors for several values of M/m_s within the M -range. Each error bar refers to the continuum extrapolation obtained fitting the three finest lattice spacings with the fit function reported in eq. (2.16). The cross point is our final SP result, which includes any residual systematic related to the choice of M/m_s . Vertically-hatched and dotted-hatched bands display the values of $\chi^{1/4}$ obtained for this temperature in, respectively, refs. [3, 4]. The former was temperature-interpolated according to the DIGA prediction $\chi^{1/4} \sim T^{-2}$ and the isospin-breaking factor was removed. The latter was mass-extrapolated according to $\chi^{1/4} \sim m_\pi$. Right: $c_{\text{SP}}/c_{\text{gluo}}$ for the several values of M/m_s within the M -range. A straight horizontal line is set at 0.

A.4 $T = 570$ MeV

The shown M -range for χ_{SP} is narrower compared to the one shown in the scatter plot of chiralities, cf. figures 18 and 19, because the mean maximum eigenvalue of D_{stag} with periodic boundaries along the time direction was smaller than the anti-periodic case.

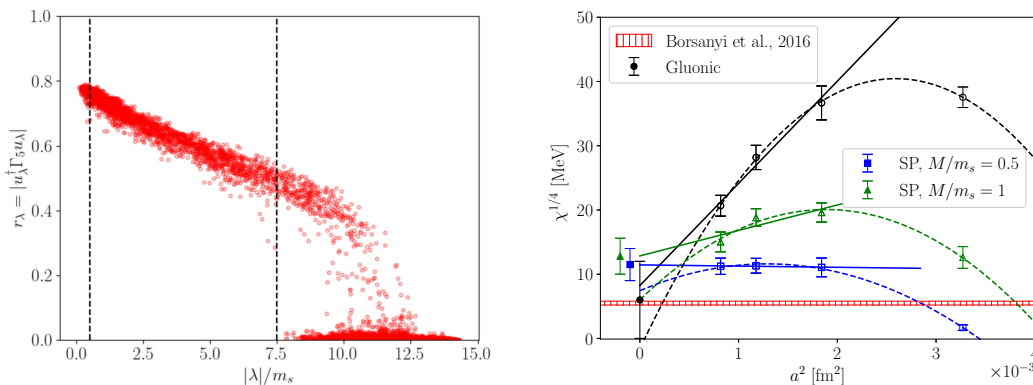


Figure 18. Left: scatter plot of the chirality r_χ vs $|\lambda|/m_s$ for our run with $a \simeq 0.0286$ fm at $T \simeq 570$ MeV. The two dashed vertical lines are set at 0.5 and 7.5 and delimit the chosen interval for M/m_s . For each reported configuration, only the first 200 eigenvalues (with the lowest magnitude) are shown. Right: comparison of the continuum limits of $\chi^{1/4}$ for $T \simeq 570$ MeV obtained with the gluonic and the SP discretizations. Vertically-hatched band displays the value of $\chi^{1/4}$ obtained for this temperature in ref. [3], which was temperature-interpolated according to the DIGA prediction $\chi^{1/4} \sim T^{-2}$ and the isospin-breaking factor was removed.

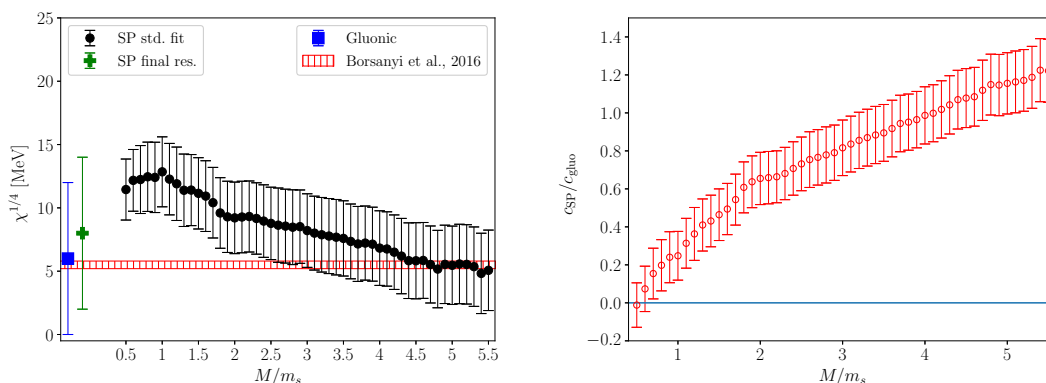


Figure 19. Left: continuum limits of $\chi^{1/4}$ obtained at $T \simeq 570$ MeV from spectral projectors for several values of M/m_s within the M -range. Each error bar refers to the continuum extrapolation obtained fitting the three finest lattice spacings with the fit function reported in eq. (2.16). The cross point is our final SP result, which includes any residual systematic related to the choice of M/m_s . Vertically-hatched band displays the value of $\chi^{1/4}$ obtained for this temperature in ref. [3], which was temperature-interpolated according to the DIGA prediction $\chi^{1/4} \sim T^{-2}$ and the isospin-breaking factor was removed. Right: $c_{\text{SP}}/c_{\text{gluo}}$ for the several values of M/m_s within the M -range. A straight horizontal line is set at 0.

Open Access. This article is distributed under the terms of the Creative Commons Attribution License ([CC-BY 4.0](https://creativecommons.org/licenses/by/4.0/)), which permits any use, distribution and reproduction in any medium, provided the original author(s) and source are credited. SCOAP³ supports the goals of the International Year of Basic Sciences for Sustainable Development.

References

- [1] C. Bonati et al., *Axion phenomenology and θ -dependence from $N_f = 2 + 1$ lattice QCD*, *JHEP* **03** (2016) 155 [[arXiv:1512.06746](https://arxiv.org/abs/1512.06746)] [[INSPIRE](#)].
- [2] J. Frison, R. Kitano, H. Matsufuru, S. Mori and N. Yamada, *Topological susceptibility at high temperature on the lattice*, *JHEP* **09** (2016) 021 [[arXiv:1606.07175](https://arxiv.org/abs/1606.07175)] [[INSPIRE](#)].
- [3] S. Borsányi et al., *Calculation of the axion mass based on high-temperature lattice quantum chromodynamics*, *Nature* **539** (2016) 69 [[arXiv:1606.07494](https://arxiv.org/abs/1606.07494)] [[INSPIRE](#)].
- [4] P. Petreczky, H.-P. Schadler and S. Sharma, *The topological susceptibility in finite temperature QCD and axion cosmology*, *Phys. Lett. B* **762** (2016) 498 [[arXiv:1606.03145](https://arxiv.org/abs/1606.03145)] [[INSPIRE](#)].
- [5] C. Bonati, M. D’Elia, G. Martinelli, F. Negro, F. Sanfilippo and A. Todaro, *Topology in full QCD at high temperature: a multicanonical approach*, *JHEP* **11** (2018) 170 [[arXiv:1807.07954](https://arxiv.org/abs/1807.07954)] [[INSPIRE](#)].
- [6] M.P. Lombardo and A. Trunin, *Topology and axions in QCD*, *Int. J. Mod. Phys. A* **35** (2020) 2030010 [[arXiv:2005.06547](https://arxiv.org/abs/2005.06547)] [[INSPIRE](#)].
- [7] R.D. Peccei and H.R. Quinn, *CP Conservation in the Presence of Instantons*, *Phys. Rev. Lett.* **38** (1977) 1440 [[INSPIRE](#)].
- [8] R.D. Peccei and H.R. Quinn, *Constraints Imposed by CP Conservation in the Presence of Instantons*, *Phys. Rev. D* **16** (1977) 1791 [[INSPIRE](#)].
- [9] F. Wilczek, *Problem of Strong P and T Invariance in the Presence of Instantons*, *Phys. Rev. Lett.* **40** (1978) 279 [[INSPIRE](#)].
- [10] S. Weinberg, *A New Light Boson?*, *Phys. Rev. Lett.* **40** (1978) 223 [[INSPIRE](#)].
- [11] J. Preskill, M.B. Wise and F. Wilczek, *Cosmology of the Invisible Axion*, *Phys. Lett. B* **120** (1983) 127 [[INSPIRE](#)].
- [12] L.F. Abbott and P. Sikivie, *A Cosmological Bound on the Invisible Axion*, *Phys. Lett. B* **120** (1983) 133 [[INSPIRE](#)].
- [13] M. Dine and W. Fischler, *The Not So Harmless Axion*, *Phys. Lett. B* **120** (1983) 137 [[INSPIRE](#)].
- [14] L. Di Luzio, M. Giannotti, E. Nardi and L. Visinelli, *The landscape of QCD axion models*, *Phys. Rept.* **870** (2020) 1 [[arXiv:2003.01100](https://arxiv.org/abs/2003.01100)] [[INSPIRE](#)].
- [15] D.J. Gross, R.D. Pisarski and L.G. Yaffe, *QCD and Instantons at Finite Temperature*, *Rev. Mod. Phys.* **53** (1981) 43 [[INSPIRE](#)].
- [16] A. Boccaletti and D. Nogradi, *The semi-classical approximation at high temperature revisited*, *JHEP* **03** (2020) 045 [[arXiv:2001.03383](https://arxiv.org/abs/2001.03383)] [[INSPIRE](#)].
- [17] O. Wantz and E.P.S. Shellard, *Axion Cosmology Revisited*, *Phys. Rev. D* **82** (2010) 123508 [[arXiv:0910.1066](https://arxiv.org/abs/0910.1066)] [[INSPIRE](#)].

- [18] E. Berkowitz, M.I. Buchoff and E. Rinaldi, *Lattice QCD input for axion cosmology*, *Phys. Rev. D* **92** (2015) 034507 [[arXiv:1505.07455](#)] [[INSPIRE](#)].
- [19] M.A. Clark and A.D. Kennedy, *Accelerating dynamical fermion computations using the rational hybrid Monte Carlo (RHMC) algorithm with multiple pseudofermion fields*, *Phys. Rev. Lett.* **98** (2007) 051601 [[hep-lat/0608015](#)] [[INSPIRE](#)].
- [20] M.A. Clark and A.D. Kennedy, *Accelerating Staggered Fermion Dynamics with the Rational Hybrid Monte Carlo (RHMC) Algorithm*, *Phys. Rev. D* **75** (2007) 011502 [[hep-lat/0610047](#)] [[INSPIRE](#)].
- [21] B. Alles, G. Boyd, M. D’Elia, A. Di Giacomo and E. Vicari, *Hybrid Monte Carlo and topological modes of full QCD*, *Phys. Lett. B* **389** (1996) 107 [[hep-lat/9607049](#)] [[INSPIRE](#)].
- [22] L. Del Debbio, G.M. Manca and E. Vicari, *Critical slowing down of topological modes*, *Phys. Lett. B* **594** (2004) 315 [[hep-lat/0403001](#)] [[INSPIRE](#)].
- [23] ALPHA collaboration, *Critical slowing down and error analysis in lattice QCD simulations*, *Nucl. Phys. B* **845** (2011) 93 [[arXiv:1009.5228](#)] [[INSPIRE](#)].
- [24] M. Lüscher and S. Schaefer, *Lattice QCD without topology barriers*, *JHEP* **07** (2011) 036 [[arXiv:1105.4749](#)] [[INSPIRE](#)].
- [25] C. Bonati and M. D’Elia, *Topological critical slowing down: variations on a toy model*, *Phys. Rev. E* **98** (2018) 013308 [[arXiv:1709.10034](#)] [[INSPIRE](#)].
- [26] C. Bonanno, C. Bonati and M. D’Elia, *Topological properties of CP^{N-1} models in the large- N limit*, *JHEP* **01** (2019) 003 [[arXiv:1807.11357](#)] [[INSPIRE](#)].
- [27] M. Lüscher, *Topological effects in QCD and the problem of short distance singularities*, *Phys. Lett. B* **593** (2004) 296 [[hep-th/0404034](#)] [[INSPIRE](#)].
- [28] L. Giusti and M. Lüscher, *Chiral symmetry breaking and the Banks-Casher relation in lattice QCD with Wilson quarks*, *JHEP* **03** (2009) 013 [[arXiv:0812.3638](#)] [[INSPIRE](#)].
- [29] M. Lüscher and F. Palombi, *Universality of the topological susceptibility in the SU(3) gauge theory*, *JHEP* **09** (2010) 110 [[arXiv:1008.0732](#)] [[INSPIRE](#)].
- [30] ETM collaboration, *Non-perturbative Test of the Witten-Veneziano Formula from Lattice QCD*, *JHEP* **09** (2015) 020 [[arXiv:1504.07954](#)] [[INSPIRE](#)].
- [31] C. Alexandrou et al., *Topological susceptibility from twisted mass fermions using spectral projectors and the gradient flow*, *Phys. Rev. D* **97** (2018) 074503 [[arXiv:1709.06596](#)] [[INSPIRE](#)].
- [32] C. Bonanno, G. Clemente, M. D’Elia and F. Sanfilippo, *Topology via spectral projectors with staggered fermions*, *JHEP* **10** (2019) 187 [[arXiv:1908.11832](#)] [[INSPIRE](#)].
- [33] B.A. Berg and T. Neuhaus, *Multicanonical ensemble: A New approach to simulate first order phase transitions*, *Phys. Rev. Lett.* **68** (1992) 9 [[hep-lat/9202004](#)] [[INSPIRE](#)].
- [34] P.T. Jahn, G.D. Moore and D. Robaina, $\chi_{top}(T \gg T_c)$ in pure-gluon QCD through reweighting, *Phys. Rev. D* **98** (2018) 054512 [[arXiv:1806.01162](#)] [[INSPIRE](#)].
- [35] C. Bonanno, M. D’Elia and F. Margari, *The topological susceptibility of the 2d CP^1 ($O(3)$ non-linear σ) model: to ∞ or not to ∞ ?*, [arXiv:2208.00185](#) [[INSPIRE](#)].
- [36] A. Laio, G. Martinelli and F. Sanfilippo, *Metadynamics surfing on topology barriers: the CP^{N-1} case*, *JHEP* **07** (2016) 089 [[arXiv:1508.07270](#)] [[INSPIRE](#)].

- [37] C. Morningstar and M.J. Peardon, *Analytic smearing of SU(3) link variables in lattice QCD*, *Phys. Rev. D* **69** (2004) 054501 [[hep-lat/0311018](#)] [[INSPIRE](#)].
- [38] Y. Aoki et al., *The QCD transition temperature: results with physical masses in the continuum limit II*, *JHEP* **06** (2009) 088 [[arXiv:0903.4155](#)] [[INSPIRE](#)].
- [39] S. Borsányi et al., *The QCD equation of state with dynamical quarks*, *JHEP* **11** (2010) 077 [[arXiv:1007.2580](#)] [[INSPIRE](#)].
- [40] S. Borsányi, Z. Fodor, C. Hölbling, S.D. Katz, S. Krieg and K.K. Szabo, *Full result for the QCD equation of state with 2 + 1 flavors*, *Phys. Lett. B* **730** (2014) 99 [[arXiv:1309.5258](#)] [[INSPIRE](#)].
- [41] P. Di Vecchia, K. Fabricius, G.C. Rossi and G. Veneziano, *Preliminary Evidence for U(1)-A Breaking in QCD from Lattice Calculations*, *Nucl. Phys. B* **192** (1981) 392 [[INSPIRE](#)].
- [42] P. Di Vecchia, K. Fabricius, G.C. Rossi and G. Veneziano, *Numerical Checks of the Lattice Definition Independence of Topological Charge Fluctuations*, *Phys. Lett. B* **108** (1982) 323 [[INSPIRE](#)].
- [43] M. Campostrini, A. Di Giacomo and H. Panagopoulos, *The Topological Susceptibility on the Lattice*, *Phys. Lett. B* **212** (1988) 206 [[INSPIRE](#)].
- [44] E. Vicari and H. Panagopoulos, *θ dependence of SU(N) gauge theories in the presence of a topological term*, *Phys. Rept.* **470** (2009) 93 [[arXiv:0803.1593](#)] [[INSPIRE](#)].
- [45] B. Berg, *Dislocations and Topological Background in the Lattice O(3) σ Model*, *Phys. Lett. B* **104** (1981) 475 [[INSPIRE](#)].
- [46] Y. Iwasaki and T. Yoshie, *Instantons and Topological Charge in Lattice Gauge Theory*, *Phys. Lett. B* **131** (1983) 159 [[INSPIRE](#)].
- [47] S. Itoh, Y. Iwasaki and T. Yoshie, *Stability of Instantons on the Lattice and the Renormalized Trajectory*, *Phys. Lett. B* **147** (1984) 141 [[INSPIRE](#)].
- [48] M. Teper, *Instantons in the Quantized SU(2) Vacuum: A Lattice Monte Carlo Investigation*, *Phys. Lett. B* **162** (1985) 357 [[INSPIRE](#)].
- [49] E.-M. Ilgenfritz, M.L. Laursen, G. Schierholz, M. Müller-Preussker and H. Schiller, *First Evidence for the Existence of Instantons in the Quantized SU(2) Lattice Vacuum*, *Nucl. Phys. B* **268** (1986) 693 [[INSPIRE](#)].
- [50] M. Campostrini, A. Di Giacomo, H. Panagopoulos and E. Vicari, *Topological Charge, Renormalization and Cooling on the Lattice*, *Nucl. Phys. B* **329** (1990) 683 [[INSPIRE](#)].
- [51] B. Alles, L. Cosmai, M. D’Elia and A. Papa, *Topology in 2-D CP^{N-1} models on the lattice: A Critical comparison of different cooling techniques*, *Phys. Rev. D* **62** (2000) 094507 [[hep-lat/0001027](#)] [[INSPIRE](#)].
- [52] APE collaboration, *Glueball Masses and String Tension in Lattice QCD*, *Phys. Lett. B* **192** (1987) 163 [[INSPIRE](#)].
- [53] M. Lüscher, *Trivializing maps, the Wilson flow and the HMC algorithm*, *Commun. Math. Phys.* **293** (2010) 899 [[arXiv:0907.5491](#)] [[INSPIRE](#)].
- [54] M. Lüscher, *Properties and uses of the Wilson flow in lattice QCD*, *JHEP* **08** (2010) 071 [*Erratum ibid.* **03** (2014) 092] [[arXiv:1006.4518](#)] [[INSPIRE](#)].
- [55] C. Bonati and M. D’Elia, *Comparison of the gradient flow with cooling in SU(3) pure gauge theory*, *Phys. Rev. D* **89** (2014) 105005 [[arXiv:1401.2441](#)] [[INSPIRE](#)].

- [56] C. Alexandrou, A. Athenodorou and K. Jansen, *Topological charge using cooling and the gradient flow*, *Phys. Rev. D* **92** (2015) 125014 [[arXiv:1509.04259](#)] [[INSPIRE](#)].
- [57] L. Del Debbio, H. Panagopoulos and E. Vicari, *θ dependence of $SU(N)$ gauge theories*, *JHEP* **08** (2002) 044 [[hep-th/0204125](#)] [[INSPIRE](#)].
- [58] C. Bonati, M. D’Elia and A. Scapellato, *θ dependence in $SU(3)$ Yang-Mills theory from analytic continuation*, *Phys. Rev. D* **93** (2016) 025028 [[arXiv:1512.01544](#)] [[INSPIRE](#)].
- [59] K.J. Maschhoff and D.C. Sorensen, *P_arpac: An efficient portable large scale eigenvalue package for distributed memory parallel architectures*, in *Applied Parallel Computing Industrial Computation and Optimization*, J. Waśniewski, J. Dongarra, K. Madsen and D. Olesen eds., Springer Berlin Heidelberg (1996), pp. 478–486 [[DOI](#)].
- [60] P. Di Vecchia and G. Veneziano, *Chiral Dynamics in the Large N Limit*, *Nucl. Phys. B* **171** (1980) 253 [[INSPIRE](#)].
- [61] H. Leutwyler and A.V. Smilga, *Spectrum of Dirac operator and role of winding number in QCD*, *Phys. Rev. D* **46** (1992) 5607 [[INSPIRE](#)].
- [62] TWQCD collaboration, *Topological Susceptibility to the One-Loop Order in Chiral Perturbation Theory*, *Phys. Rev. D* **80** (2009) 034502 [[arXiv:0903.2146](#)] [[INSPIRE](#)].
- [63] F.-K. Guo and U.-G. Meißner, *Cumulants of the QCD topological charge distribution*, *Phys. Lett. B* **749** (2015) 278 [[arXiv:1506.05487](#)] [[INSPIRE](#)].
- [64] G. Grilli di Cortona, E. Hardy, J. Pardo Vega and G. Villadoro, *The QCD axion, precisely*, *JHEP* **01** (2016) 034 [[arXiv:1511.02867](#)] [[INSPIRE](#)].
- [65] F. Luciano and E. Meggiolaro, *Study of the theta dependence of the vacuum energy density in chiral effective Lagrangian models at zero temperature*, *Phys. Rev. D* **98** (2018) 074001 [[arXiv:1806.00835](#)] [[INSPIRE](#)].
- [66] A. Alexandru and I. Horváth, *Possible New Phase of Thermal QCD*, *Phys. Rev. D* **100** (2019) 094507 [[arXiv:1906.08047](#)] [[INSPIRE](#)].
- [67] A. Alexandru and I. Horváth, *Unusual Features of QCD Low-Energy Modes in the Infrared Phase*, *Phys. Rev. Lett.* **127** (2021) 052303 [[arXiv:2103.05607](#)] [[INSPIRE](#)].
- [68] A.Y. Kotov, M.P. Lombardo and A. Trunin, *QCD transition at the physical point, and its scaling window from twisted mass Wilson fermions*, *Phys. Lett. B* **823** (2021) 136749 [[arXiv:2105.09842](#)] [[INSPIRE](#)].
- [69] M. Cardinali, M. D’Elia and A. Pasqui, *Thermal monopole condensation in QCD with physical quark masses*, [arXiv:2107.02745](#) [[INSPIRE](#)].
- [70] M. Hasenbusch, *Fighting topological freezing in the two-dimensional CP^{N-1} model*, *Phys. Rev. D* **96** (2017) 054504 [[arXiv:1706.04443](#)] [[INSPIRE](#)].
- [71] M. Berni, C. Bonanno and M. D’Elia, *Large- N expansion and θ -dependence of 2d CP^{N-1} models beyond the leading order*, *Phys. Rev. D* **100** (2019) 114509 [[arXiv:1911.03384](#)] [[INSPIRE](#)].
- [72] C. Bonanno, C. Bonati and M. D’Elia, *Large- N $SU(N)$ Yang-Mills theories with milder topological freezing*, *JHEP* **03** (2021) 111 [[arXiv:2012.14000](#)] [[INSPIRE](#)].
- [73] C. Bonanno, M. D’Elia, B. Lucini and D. Vadicchino, *Towards glueball masses of large- N $SU(N)$ pure-gauge theories without topological freezing*, *Phys. Lett. B* **833** (2022) 137281 [[arXiv:2205.06190](#)] [[INSPIRE](#)].